atmosphere

Article

Feasibility of Retrieving Stratospheric Aerosol Extinction Fields from GEO–LEO Limb Measurements: An Inversion Algorithm Approach

Alexandru Doicu [1], Dmitry S. Efremenko [2,*], Dirk Giggenbach [3] and Adrian Doicu [2]

[1] Independent Researcher, 82110 Germering, Germany
[2] Remote Sensing Technology Institute (IMF), German Aerospace Center (DLR), 82234 Wessling, Germany
[3] Institute of Communications and Navigation (IKN), German Aerospace Center (DLR), 82234 Wessling, Germany
* Correspondence: dmitry.efremenko@dlr.de

Abstract

This paper investigates the feasibility of retrieving stratospheric aerosol extinction fields from GEO–LEO limb measurements using a dedicated inversion framework. The retrieval problem is severely ill-posed and involves a fundamentally three-dimensional observation geometry. To obtain stable solutions, variations of the extinction field in the cross-track direction are neglected, reducing the problem to the retrieval of radial and weakly horizontally varying aerosol distributions within a quasi-planar GEO–LEO geometry. Two simplified retrieval strategies are considered. In the first strategy, the radial extinction profile and the horizontal extent of the aerosol field are retrieved using external aerosol optical thickness observations as additional constraints. In the second strategy, the extinction field is represented by a parametric model and the corresponding model parameters are retrieved. To reduce the computational complexity, a simplified single-scattering forward model is adopted. The inversion problem is formulated as the minimization of a regularized Tikhonov function and is solved using a multistart optimization framework combining global random sampling, validation and selection of admissible starting points, local bounded optimization, discrepancy-principle filtering, and clustering of candidate solutions. Numerical simulations for a broad range of synthetic aerosol scenarios show that the proposed methodology is capable of reproducing the dominant aerosol structures with good accuracy. Although the retrieval problem remains strongly ill-conditioned, the effective degrees of freedom indicate that GEO–LEO limb measurements contain substantial independent information about the aerosol field and provide a promising basis for retrieving both radial aerosol extinction profiles and aspects of their horizontal structure.

Keywords: stratospheric aerosols; aerosol extinction; GEO–LEO limb measurements; limb sounding; inverse problems; Tikhonov regularization; remote sensing

Academic Editors: Florin Unga and Marius M. Cazacu

Received: 24 June 2026
Revised: 24 July 2026
Accepted: 28 July 2026
Published: 29 July 2026

1. Introduction

Stratospheric aerosol retrievals from passive limb measurements play an important role in atmospheric remote sensing and climate research. Several satellite limb-scatter instruments, including SCIAMACHY, OSIRIS, OMPS-LP, and the BLS instrument onboard Tiangong-2, have been developed to retrieve aerosol extinction profiles from scattered solar radiation [1–9]. Most existing retrieval algorithms assume horizontal homogeneity or local spherical symmetry along the line of sight, so that the aerosol extinction depends

 https://doi.org/10.3390/atmos17080737

only on the radial coordinate, e R, $\sigma = \sigma(R)$, [1–5]. Although this approximation greatly simplifies the retrieval problem, it may introduce systematic errors when horizontally localized aerosol structures are present. Previous studies have shown that such errors can be reduced by incorporating independent information on the horizontal extent of the aerosol field; for example, from nadir aerosol optical thickness (AOT) measurements [1].

Geostationary satellites (GEOs) operating on nearly circular orbits play a central role in modern communication. These satellites are positioned at an altitude of approximately 35,786 km above the equator, with the same period as Earth's rotation. Thus, they remain fixed over a ground nadir point and are seen at a constant position in the sky, independent from time of day or season. Due to this prominent characteristic, GEOs can serve as relays for data repatriation from low-Earth-orbit (LEO) satellites. A particular implementation of an optical GEO-LEO relays is the European Data Relay System (EDRS) which consists of geostationary satellites (Alphasat-TDP-1, EDRS-A, and EDRS-C), receiving data via optical inter-satellite links (OISL) from Earth-observation satellites in LEO (Sentinel-1A and others) [10]. The EDRS operates links at a signal wavelength of 1064nm. With optical terminal apertures of 135 mm diameter, they allow a beam divergence of around 8.4 µrad FWHM [11]. After bridging the GEO-LEO distance, this small beam divergence enables a rather strong received power at the counter terminal of more than 100 nW.

Besides the 1064 nm technology of EDRS, other laser wavelengths and modulation formats are applied in OISL scenarios (mostly 1550 nm and 850 nm) [12]. It has been proposed to execute metrology tasks in parallel to OISL data comms, using the link hardware in a sensor mode [13]. While ample link margin is available for executing the metrology task covering also atmospheric attenuation, there is no need to additionally secure the data communications quality when focusing only on the sensing task. Preceding grazing experiments show a major impact of index-of-refraction turbulence (IRT) on the signal stability [14], and pure measurements of power transmission are expected to show a significant response to the aerosol and molecular absorption due to the long horizontal path section during grazing.

In contrast to GEOs, low-Earth-orbit (LEO) satellites operate at altitudes typically ranging from approximately only 300 km to 2000 km which allows high-resolution observations of ground or atmospheric features. They move rapidly relative to the Earth surface, typically completing one orbit within about 90 to 120 min.

Many Earth-observation missions employ near-polar or Sun-synchronous (SSO) LEO orbits in order to achieve near-global coverage through successive orbital passes. Representative examples include the polar MetOp satellite fleet, or ESA's several Sentinel missions. In the context of the present study, we consider observations at a wavelength of 1064 nm, with received power levels as necessary for the OISL data communication link in EDRS. A major benefit of this wavelength is the lack of absorption lines from atmospheric molecules, which would otherwise falsify the grazing measurements of aerosol absorption [15].

The GEO-LEO OISL geometry is specifically advantageous for atmospheric sounding applications as it features consecutive grazing measurements with lowering altitudes, over approximately a fixed geographic location (slight horizontal shifts apply), as will be described in more detail later. Figure 1 illustrates this GEO–LEO grazing geometry for representative Alphasat-TDP1–Sentinel-1A link events.

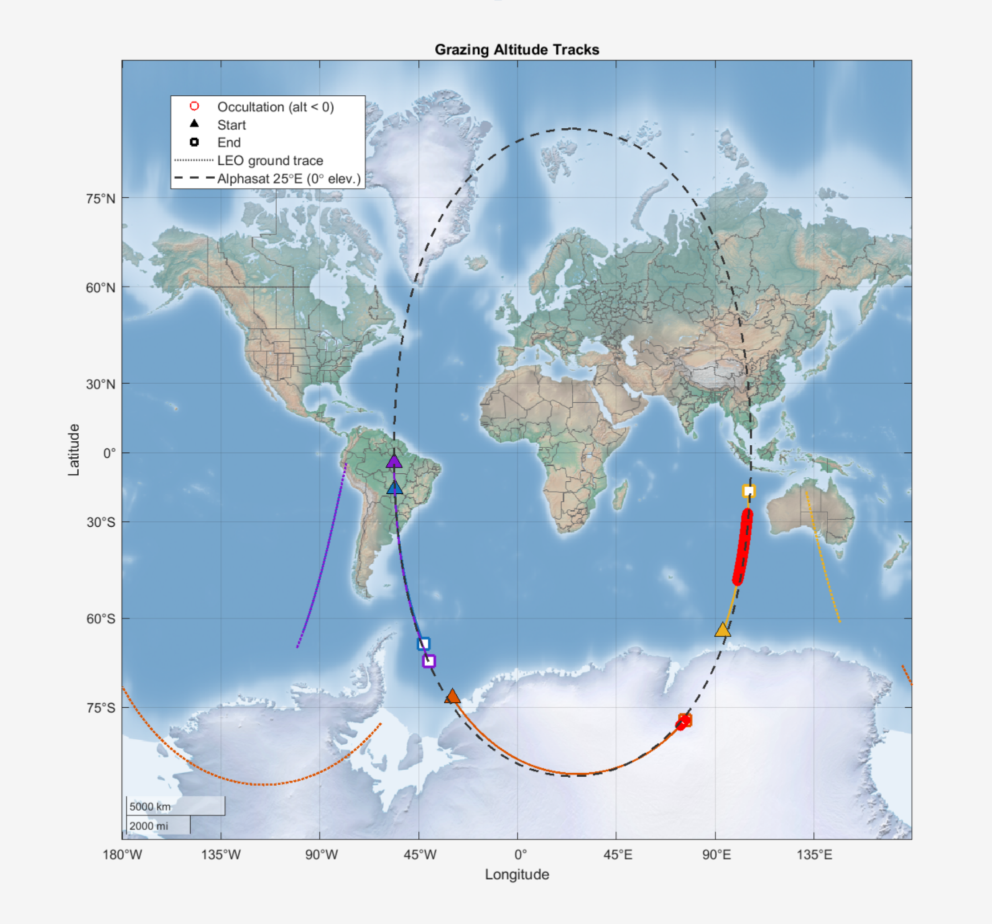

Figure 1. Exemplary geometry of GEO–LEO optical inter-satellite links with atmospheric grazing. The map shows representative LEO ground tracks, occultation or grazing segments, and the approximate line-of-sight geometry for links between Alphasat-TDP1 and Sentinel-1A. Such geometries provide consecutive measurements at decreasing grazing altitudes over approximately fixed geographic regions, making them suitable for atmospheric sounding applications.

When the line of sight connecting a GEO and a LEO satellite intersects the atmosphere tangentially, a limb-observation geometry is formed. As the LEO satellite moves along its orbit, the tangent point evolves continuously in altitude and geographic location, while the GEO platform remains nearly stationary relative to the Earth surface. The resulting sequence of limb measurements samples different regions of the atmosphere and contains information about the spatial distribution of atmospheric constituents and aerosols. The large separation between the two satellites produces long atmospheric limb paths and therefore enhances sensitivity to weak extinction signals in the stratosphere. At the same time, the combination of a nearly fixed GEO platform and a moving LEO platform provides a diverse set of viewing geometries that may contain information about the horizontal structure of the aerosol extinction field.

The present work builds upon the concept introduced by Dörner et al. [1] of using independent nadir AOT observations to constrain the horizontal extent of the aerosol field. Here, this idea is extended to a GEO–LEO limb-occultation framework. Unlike conventional passive limb-scatter retrievals, which reconstruct one-dimensional extinction profiles under the assumption of horizontal homogeneity, the proposed methodology combines limb observations with AOT constraints to reconstruct aspects of the horizontal aerosol structure. This represents a first step toward two-dimensional aerosol retrievals from GEO–LEO limb measurements.

Most passive limb-scatter retrieval algorithms employ Bayesian inversion methods, which, under Gaussian assumptions for the measurement errors and prior information, are closely related to classical Tikhonov regularization, e.g., [2,16]. These methods are generally applicable when the inverse problem is not excessively ill-posed. In contrast, the GEO–LEO retrieval problem considered here is strongly nonlinear and severely ill-posed. This motivates the development of a specialized inversion approach. Accordingly, the retrieval problem is formulated as a regularized optimization problem and solved using a multistart optimization strategy tailored to nonlinear ill-posed inverse problems.

This study is organized as follows. Section 2 introduces the GEO–LEO observation geometry, retrieval domain, forward model, inverse formulation, regularization strategy, and numerical optimization procedure. Numerical retrieval results for several synthetic aerosol scenarios are then presented and analyzed.

2. Retrieval Methodology

2.1. GEO–LEO Observation Geometry and Retrieval Domain

Figure 2 introduces the GEO–LEO observation geometry and the retrieval domain used throughout this work. The upper panel illustrates the reference frames and orbital parameters employed to describe the relative positions of the GEO and LEO satellites. The inertial frame $OXYZ$ is centered at the Earth center, with the Z-axis aligned with the Earth rotation axis. The Earth-fixed frame $Ox_{\mathrm{E}}y_{\mathrm{E}}z_{\mathrm{E}}$ is obtained by a rotation around the Z-axis through the Earth rotation angle ϕ_{E}, and is used to determine geographic coordinates. The LEO orbital plane is constructed by first rotating the inertial frame around the Z-axis by the right ascension of the ascending node Ω, which defines the line of nodes, and then rotating around this line by the inclination angle I. The orbital angular coordinate u specifies the position of the LEO satellite within the orbital plane. Thus, Ω and I determine the orientation of the orbital plane, while u determines the instantaneous satellite position.

The middle panel of Figure 2 defines the retrieval domain used in the inversion. The line of sight follows a limb path, and each ray is characterized by a tangent point, i.e., the point of closest approach to the Earth's surface. The lowest tangent radius is R_{Tmin}, and we define an upper tangent radius R_{Tmax}, above which the aerosol extinction field can be assumed to be negligible. The retrieval domain is indicated by the grid points highlighted in red. It consists of all atmospheric points that are intersected by the set of limb rays corresponding to polar angles θ in the range $\theta \in [\theta_{\min}, \theta_{\max}]$ and radial distances R between $R_{\min}(\theta)$ and $R_{\max} = R_{\mathrm{Tmax}}$. Thus, the retrieval domain is given by

$$\Omega = \{(R, \theta) \mid \theta_{\min} \leq \theta \leq \theta_{\max}, \quad R_{\min}(\theta) \leq R \leq R_{\max}\}.$$

The lower radial boundary $R_{\min}(\theta)$ is defined by $R_{\min}(\theta) = R_{\mathrm{Tmin}} / \cos(\theta_{\mathrm{T}} - \theta)$, where $\theta_{\mathrm{T}} = \pi/2 - \beta$, $\beta = \arcsin(R_{\mathrm{Tmin}}/R_{\mathrm{G}})$, and R_{G} is the GEO orbital radius. The angles $\theta_{\min}$ and $\theta_{\max}$ are determined by the intersection of the line of sight corresponding to the lowest tangent radius R_{Tmin} with the circle of radius $R_{\max}$. It should be pointed out that, in this construction, the retrieval domain is determined by the prescribed tangent radii R_{Tmin} and R_{Tmax}, together with the GEO orbital radius R_{G}. Consequently, the angular limits $\theta_{\min}$ and $\theta_{\max}$ are fixed geometric quantities and are not redefined for each instantaneous GEO–LEO observation plane. In other words, the retrieval domain is treated as fixed for all instantaneous GEO–LEO observation planes.

The lower panel of Figure 2 illustrates how the tangent altitude determines the atmospheric region sampled by each GEO–LEO limb measurement. The horizontal line indicates the upper boundary of the retrieval domain, while the retrieval region itself is confined to the altitude interval between approximately 8 km and 28 km, where the aerosol extinction is assumed to be significant. It can be seen that lower tangent altitudes correspond to limb rays penetrating deeper into the atmosphere and exhibiting stronger curvature near the tangent point. At the same time, the tangent points remain nearly identical for the different limb paths, indicating that the measurements are approximately localized around the same atmospheric column.

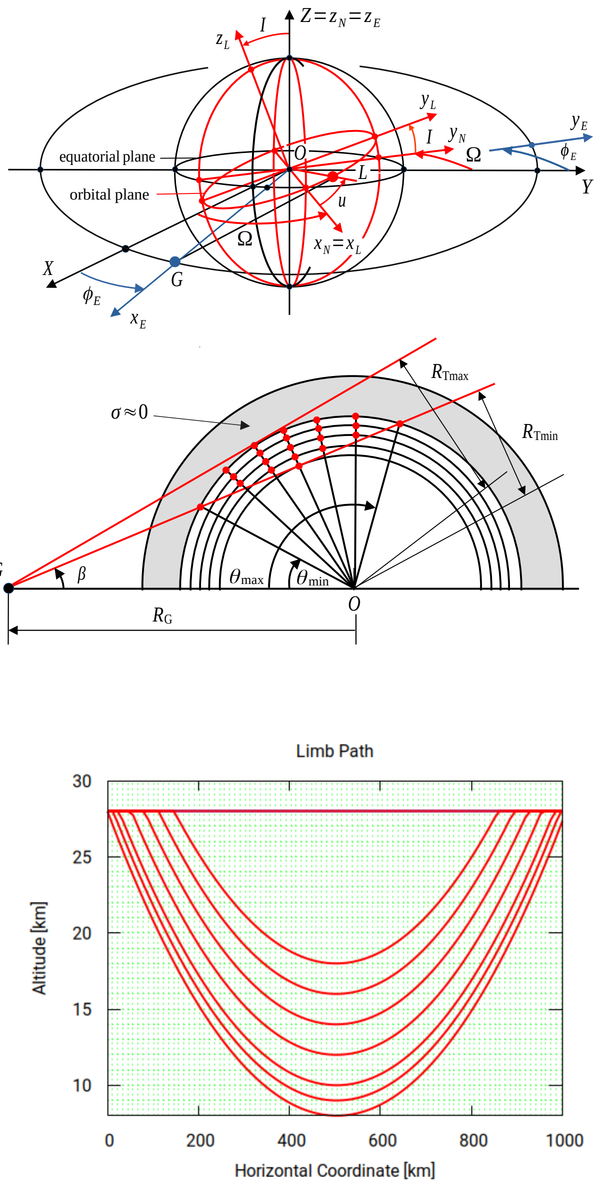

Figure 2. Observation geometry for a GEO–LEO limb retrieval configuration. (**Top**) Three-dimensional GEO–LEO observation geometry showing the GEO satellite G, the LEO satellite L, the LEO orbital plane, the equatorial plane, the right ascension of the ascending node Ω, the orbital inclination I, and the orbital angular coordinate u. (**Middle**) Retrieval geometry in polar coordinates, with tangent-height range $R_{\mathrm{Tmin}} \leq R_{\mathrm{T}} \leq R_{\mathrm{Tmax}}$ and angular retrieval interval $\theta_{\mathrm{min}} \leq \theta \leq \theta_{\mathrm{max}}$. (**Bottom**) Limb paths corresponding to different tangent altitudes.

The retrieval formulation developed in this work relies on two key geometric assumptions.

1. First, the observation plane should evolve only slowly during a single occultation so that all measurements can be represented within a common retrieval plane.
2. Second, the tangent points should remain sufficiently localized during an individual occultation to ensure that the measurements probe approximately the same atmospheric column.

At the same time, successive occultations should provide broad geographic coverage over longer observation periods. These assumptions are assessed numerically using the geometric relations derived in Appendix A. The corresponding analyses are presented in Table 1 and Figures 3 and 4.

Table 1 reports the measurement time t_{mes} and the maximum angle ψ_{max} between instantaneous GEO–LEO observation planes for different orbital inclinations I and right ascensions of the ascending node Ω. The small values of ψ_{max}, all below approximately 1°, confirm that the observation plane evolves only slowly during a single occultation. This supports the quasi-planar approximation adopted in the retrieval model.

Figure 3 illustrates the temporal evolution of the tangent altitude together with the latitude and longitude of the Earth-surface projection of the tangent point over a 48 h observation period. The tangent altitudes repeatedly span the prescribed retrieval interval, while the tangent-point coordinates exhibit the expected quasi-periodic variation associated with the relative motion of the GEO and LEO satellites. During an individual occultation the longitude variations remain comparatively small, indicating that the measurements sample approximately the same atmospheric column. Over successive occultations, however, the tangent points migrate to different geographic locations, thereby providing the spatial coverage required for the retrieval concept.

Figure 4 is used to examine the long-term geographic coverage of the tangent-point projections over a 14-day observation period for two orbital inclinations, $I = 70^\circ$ and $I = 97^\circ$, and three values of the right ascension of the ascending node (RAAN). The simulations indicate that the long-term coverage is governed primarily by the orbital inclination, whereas the influence of the right ascension of the ascending node is comparatively small. For $I = 70^\circ$, the tangent-point projections are concentrated in two narrow longitude sectors centered approximately at $\pm 70^\circ$. Within these sectors, the observations span a broad latitude range extending from about -75° to $+75^\circ$. Consequently, this configuration provides repeated observations over large portions of the latitude range but only within limited longitude intervals. In contrast, for the near-polar orbit with $I = 97^\circ$, the tangent-point projections form two extended high-latitude bands that cover a much broader longitude range. The observations are concentrated primarily at latitudes above approximately $+50^\circ$ in the Northern Hemisphere and below approximately -50° in the Southern Hemisphere. This configuration therefore provides repeated sampling of Arctic and Antarctic regions over a wide range of longitudes. The comparison illustrates a trade-off between latitude and longitude coverage. The configuration with $I = 70^\circ$ provides access to a wider range of latitudes but only within narrow longitude corridors, whereas the near-polar configuration with $I = 97^\circ$ offers substantially broader longitude coverage at high latitudes. Furthermore, the close overlap of the results corresponding to different RAAN values indicates that the long-term geographic coverage is only weakly sensitive to the orientation of the orbital plane.

Overall, the simulations demonstrate that the GEO–LEO geometry possesses the key characteristics required by the proposed retrieval methodology. The observation plane remains nearly constant during an occultation, and the tangent points remain sufficiently localized to probe approximately the same atmospheric column. These properties justify the geometric assumptions underlying the inversion procedure and provide the foundation for retrieving not only radial aerosol extinction profiles but also aspects of the horizontal aerosol structure.

Table 1. Measurement time t_{mes} and the maximum angle ψ_{max} between the instantaneous GEO–LEO observation planes, for different inclinations I of the LEO orbital plane, and different right ascensions of the ascending node Ω.

I [°]	Ω [°]	t_{mes} [s]	ψ_{max} [°]
70	30	7	0.14
	45	9	0.31
	60	14	0.74
97	30	8	0.17
	45	8	0.30
	60	15	0.84

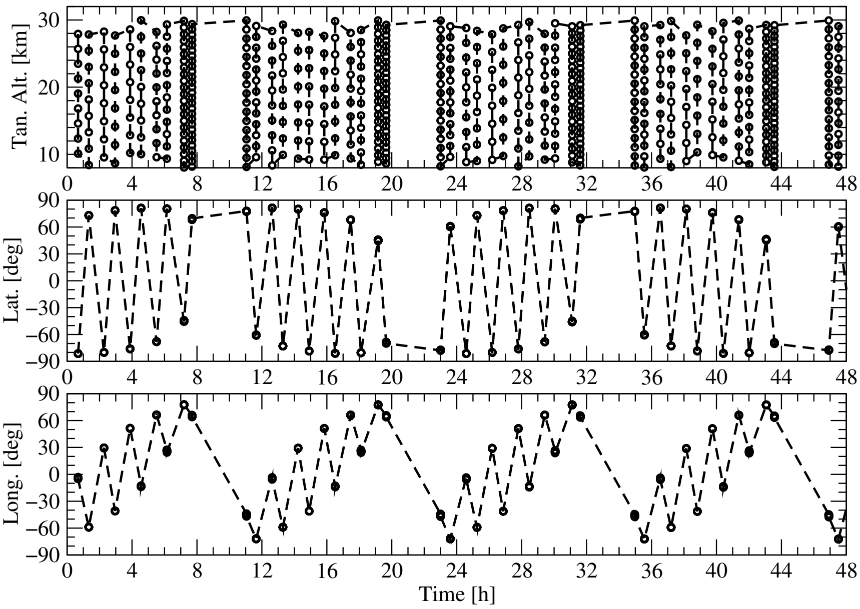

Figure 3. Temporal evolution of the tangent altitude and of the latitude and longitude of the tangent-point Earth-surface projection, for the GEO–LEO configuration. The analysis corresponds to $I = 97°$ and $\Omega = 45°$.

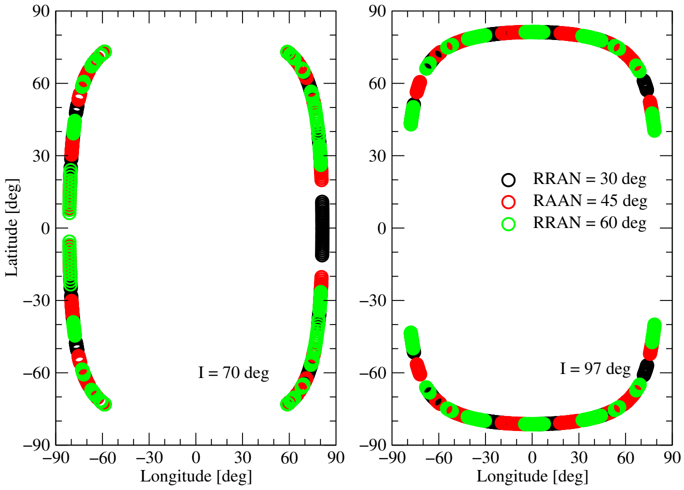

Figure 4. Cumulative geographic coverage of the GEO–LEO configuration over an observation period of 14 days. The analysis is shown for orbital inclinations $I = 70°$ and $I = 97°$, and for three values of the right ascension of the ascending node (RAAN): 30°, 45°, and 60°.

2.2. Forward Radiative Transfer Model

The radiative transfer equation for weakly focused Gaussian beams propagating through scattering media was derived by Doicu et al. [17] from Maxwell's equations. Applying the Fourier transform with respect to the horizontal coordinates reduces the three-dimensional radiative transfer equation to a sequence of one-dimensional equations in Fourier (spectral) space. Several numerical methods have been developed for solving the resulting spectral radiative transfer equation. For homogeneous slabs, discrete-ordinate formulations based on matrix-exponential [18] and eigenvalue techniques [19] have been proposed. The Spectral Spherical Harmonic Discrete Ordinate Method (SSHDOM) [20] was developed for radiative transfer in inhomogeneous three-dimensional atmospheres containing cloud layers and is particularly suitable for airborne measurement geometries. The method solves the radiative transfer equation independently for each Fourier mode using the SHDOM methodology of Evans [21,22]. In our recent work [23], the methodology was extended to space-borne lidar geometries, for which atmospheric domains extend over several tens of kilometers while the Gaussian beam footprint remains only a few tens of meters. Two independent numerical solvers were developed: an efficient Fourier-space SHDOM implementation based on Picard iteration and an independent generalized discrete-ordinate matrix-exponential solver.

As an alternative to these complete radiative-transfer models, small-angle multiple-scattering theories [24,25] describe the coupled evolution of the spatial and angular radiance distributions for narrow beams propagating through strongly forward-scattering media. Because these models account for multiple scattering at substantially lower computational cost than the complete radiative-transfer equation, they provide an attractive intermediate approximation. For completeness, the small-angle approximation is summarized in Appendix B.

The primary objective of the present work is to investigate the feasibility of retrieving stratospheric aerosol extinction fields from GEO–LEO observations. To focus on the essential aspects of the retrieval problem, several simplifying assumptions are adopted in the forward radiative transfer model. First, the atmospheric extinction is assumed to originate exclusively from aerosols. Absorption by the atmospheric gases N_2, O_2, H_2O, CO_2, and CH_4 is neglected because, at the operating wavelength of 1064 nm, these gases exhibit only weak absorption. In addition, molecular (Rayleigh) scattering by N_2 and O_2 is ignored. Consequently, the extinction field retrieved in this study is interpreted as a pure aerosol extinction field.

A second simplifying assumption concerns the treatment of scattering. The forward model is based on the single-scattering approximation, whereby only the attenuated direct beam and the corresponding single-scattering contribution are taken into account. This approximation is not universally applicable because it neglects multiple-scattering effects. Nevertheless, it is appropriate for the present proof-of-concept study for two reasons.

1. *Computational efficiency*. Solving the nonlinear inverse problem for a three-dimensional aerosol extinction field requires repeated evaluations of the forward model together with the derivatives of the simulated radiances with respect to the extinction field (the linearized forward model or Jacobian). The computation of these quantities for a complete multiple-scattering model, even within the framework of the small-angle approximation, would substantially increase the computational cost of the inversion. The single-scattering approximation therefore provides a computationally efficient forward model for the iterative optimization procedure.
2. *Applicability to the considered scenario*. The present study is concerned with the retrieval of stratospheric aerosol extinction fields in the altitude range from 8 km to 30 km, where the aerosol optical thickness is typically small and the influence of both surface

reflection and multiple scattering is expected to be comparatively weak. The accuracy of the single-scattering approximation was assessed in our recent study [23], in which the complete multiple-scattering problem was solved using two independent numerical methods. Even for a cloud with an optical thickness of 10, the detector-plane radiances computed with and without multiple scattering differed primarily by an overall scaling factor of approximately 1.06, corresponding to an error of only about 6% in the detector signal. Since the stratospheric aerosol layers considered here are substantially less optically dense than such clouds, the expected influence of multiple scattering is even smaller. Furthermore, to assess the robustness of the inversion algorithm with respect to forward-model errors, the numerical simulations presented in Section 3 include a conservative 10% systematic modelling error by scaling the synthetic measurements by a factor of 1.1 (see Section 3.2). This perturbation exceeds the estimated error due to neglecting multiple scattering and therefore provides a conservative assessment of the retrieval performance.

In the present study, the limb paths are approximated by straight-line trajectories. Thus, refractive effects associated with atmospheric gradients of the refractive index are neglected. The radiative transfer equation for the diffuse single-scattering radiance I then takes the form

$$\frac{\partial I}{\partial s}(s) = -\sigma(s)[I(s) - J(s)], \tag{1}$$

where s is the path coordinate, and σ is the (volume) extinction coefficient. The single-scattering source function is defined as

$$J(s) = \frac{\omega}{4\pi} P(\widehat{\mathbf{\Omega}}, \widehat{\mathbf{\Omega}}_0) I_{\mathrm{b}}(s), \tag{2}$$

where ω is the single scattering albedo, and P is the phase function, depending on the scattering direction $\widehat{\mathbf{\Omega}}$ and the propagation direction of the Gaussian beam $\widehat{\mathbf{\Omega}}_0$. For an axial beam, we consider a field of unit amplitude, expressed as

$$I_{\mathrm{b}}(s) = \mathrm{e}^{-\int_0^s \sigma(s')\,\mathrm{d}s'}. \tag{3}$$

In this approximation, the Gaussian beam is represented solely by its central ray. The finite beam width, angular divergence, and the redistribution of radiation caused by multiple scattering are neglected. For a layer with thickness s, the integral form of the radiative transfer equation is

$$I(s) = I(0)\mathrm{e}^{-\tau(s)} + \int_0^s \sigma(s')J(s')\mathrm{e}^{-\int_{s'}^s \sigma(u)\,\mathrm{d}u}\,\mathrm{d}s'. \tag{4}$$

Assuming that both the extinction coefficient and the product σJ vary linearly across the layer, the solution can be written as [21,22]

$$I(s) = I(0)\mathrm{e}^{-\tau} + \frac{1-\mathrm{e}^{-\tau}}{\sigma_0+\sigma_1}\left[\sigma_0 J_0 + \sigma_1 J_1 + \frac{2\sigma_0\sigma_1}{\sigma_0+\sigma_1}(J_1 - J_0)\left(1 - \frac{2}{\tau} + \frac{2\mathrm{e}^{-\tau}}{1-\mathrm{e}^{-\tau}}\right)\right], \tag{5}$$

where

$$\tau = \frac{1}{2}(\sigma_0 + \sigma_1)s \tag{6}$$

is the optical thickness across the layer, σ_0 and J_0 denote the values of the extinction coefficient and the source function at the entry point of the layer, and σ_1 and J_1 denote the corresponding values at the exit point.

For a limb path discretized into N points, we obtain the following recurrence relation:

$$I_{p+1} = I_p \mathrm{e}^{-\Delta\tau_p} + a_p \mathrm{e}^{-\tau_p}, \quad p = 1, \ldots, N-1, \quad I_1 = 0, \tag{7}$$

where I_p denotes the single-scattering radiance at point p,

$$\Delta\tau_p = \frac{1}{2}(\sigma_p + \sigma_{p+1})(s_{p+1} - s_p)$$

is the optical thickness across the segment between points p and $p+1$, σ_p and τ_p are the extinction coefficient and the cumulative optical thickness at point p, respectively, and s_p is the path coordinate measured from the GEO satellite. The coefficient a_p is given by

$$\begin{aligned} a_p = \frac{\omega}{4\pi} P(0) \frac{1 - \mathrm{e}^{-\Delta\tau_p}}{\sigma'_p + \sigma_{p+1}} \Big[\sigma'_p + \sigma_{p+1} \mathrm{e}^{-\Delta\tau_p} \\ - \frac{2\sigma'_p \sigma_{p+1}}{\sigma'_p + \sigma_{p+1}} (1 - \mathrm{e}^{-\Delta\tau_p}) \left(1 - \frac{2}{\Delta\tau_p} + \frac{2\mathrm{e}^{-\Delta\tau_p}}{1 - \mathrm{e}^{-\Delta\tau_p}} \right) \Big] \end{aligned} \tag{8}$$

where $P(0)$ is the phase function evaluated in the forward direction, and the auxiliary quantity σ'_p is defined by

$$\sigma'_p = \sigma_{p+1} + 4 \frac{\sigma_p - \sigma_{p+1}}{\Delta\tau_p}. \tag{9}$$

A stable representation for the single-scattering radiance at the exiting point N is given by

$$I_N = \mathrm{e}^{-\sum_{k \neq k_0}^{N-1} \Delta\tau_k} \sum_{p=1}^{N-1} b_p, \tag{10}$$

where the sum $\sum_{k \neq k_0}^{N-1}$ denotes the summation over $k = 1, \ldots, N-1$, excluding the index k_0 , defined by

$$\Delta\tau_{k_0} = \max_{1 \le k \le N-1} \Delta\tau_k, \tag{11}$$

and the coefficients b_p are computed as

$$b_p = a_p \mathrm{e}^{-(\Delta\tau_{k_0} - \Delta\tau_p)}. \tag{12}$$

Taking into account that the attenuated direct beam at the exit point N is given by

$$I_{\mathrm{b}N} = \mathrm{e}^{-\sum_{k=1}^{N-1} \Delta\tau_k}, \tag{13}$$

we obtain the following representation for the total signal measured by the detector:

$$I_{\mathrm{T}} = I_N + I_{\mathrm{b}N} = \mathrm{e}^{-\sum_{k \neq k_0}^{N-1} \Delta\tau_k} \left(\mathrm{e}^{-\Delta\tau_{k_0}} + \sum_{p=1}^{N-1} b_p \right). \tag{14}$$

For solving the inverse problem, we take the logarithm of the above expression, and define the forward model as

$$F(\sigma_1, \ldots, \sigma_N) = \sum_{k \neq k_0}^{N-1} \Delta\tau_k - \ln \left(\mathrm{e}^{-\Delta\tau_{k_0}} + \sum_{p=1}^{N-1} b_p \right). \tag{15}$$

In the following, in order to distinguish the extinction values along the limb path from the extinction field defined on the retrieval grid, we denote the limb-path extinction values by $\sigma_{\mathrm{L}k}, k = 1, \ldots, N$. Accordingly, the forward model is written in the form $F(\sigma_{\mathrm{L}1}, \ldots, \sigma_{\mathrm{L}N})$.

2.3. Retrieval Strategies for the Extinction Field

The retrieval of the extinction field, and in particular of the aerosol extinction field, from GEO–LEO measurements requires the solution of a three-dimensional inverse problem. To reduce the complexity of the problem, several restrictive assumptions are introduced.

First, variations of the extinction field in the cross-track direction, associated with the temporal evolution of the GEO–LEO observation geometry, are neglected. Under this assumption, the extinction field is approximated by a two-dimensional distribution in a quasi-planar GEO–LEO geometry. Even with this simplification, the retrieval of a completely general two-dimensional extinction field remains severely ill-conditioned. To assess the feasibility of such an unrestricted retrieval, a series of preliminary numerical experiments was performed using representative synthetic extinction fields. Figure 5 illustrates the idealized case in which the synthetic measurements lie exactly in the range of the forward-model operator. In this case, the prescribed extinction fields are recovered with reconstruction errors below 1%, demonstrating the correctness of the inversion algorithm. Additional numerical experiments revealed that perturbations of the synthetic measurements by less than 1% increase the reconstruction errors to more than 40%. This pronounced sensitivity indicates that the unrestricted retrieval problem is not sufficiently robust for practical applications.

For this reason, the present work does not attempt to retrieve an arbitrary extinction field. Instead, two simplified retrieval strategies are considered:

1. *Radial-grid retrieval*. The radial extinction profile and its horizontal extent are retrieved under the assumption that the radial profile is independent of the horizontal coordinate within the aerosol support region.
2. *Parametric retrieval*. The extinction field within the retrieval domain is represented by a parametric model, and the corresponding model parameters are retrieved.

2.3.1. Radial-Grid Extinction Retrieval

This section presents the mathematical framework for the radial-grid extinction retrieval. We introduce the retrieval model, formulate the corresponding inverse problem, describe the regularization strategy, and incorporate external AOT information through physically motivated retrieval constraints.

Retrieval Model

Let $\sigma(R, \theta)$ denote the extinction field in polar coordinates within an instantaneous GEO–LEO observation plane. We consider a uniform discretization $\{R_j\}_{j=1}^{N_R}$ of the radial interval $[R_{\text{Tmin}}, R_{\text{Tmax}}]$, defined by $R_j = R_{\text{Tmin}} + (j-1)\Delta R$, $j = 1, \ldots, N_R$, where $\Delta R = (R_{\text{Tmax}} - R_{\text{Tmin}})/(N_R - 1)$. Similarly, we consider a uniform discretization $\{\theta_i\}_{i=1}^{N_\theta}$ of the angular interval $[\theta_{\min}, \theta_{\max}]$, defined by $\theta_i = \theta_{\min} + (i-1)\Delta\theta$, $i = 1, \ldots, N_\theta$, where $\Delta\theta = (\theta_{\max} - \theta_{\min})/(N_\theta - 1)$. Within the geometrically admissible interval $[\theta_{\min}, \theta_{\max}]$, we assume that the aerosol layer occupies a smaller angular region $\theta_{\min}^{\text{ret}} \le \theta \le \theta_{\max}^{\text{ret}}$, where $\theta_{\min}^{\text{ret}}$ and $\theta_{\max}^{\text{ret}}$ are treated as unknown retrieval parameters. However, instead of retrieving the two bounds directly, we introduce the parameterization

$$\overline{\theta} = \frac{1}{2}(\theta_{\min}^{\text{ret}} + \theta_{\max}^{\text{ret}}), \;\; \Theta = \frac{1}{2}(\theta_{\max}^{\text{ret}} - \theta_{\min}^{\text{ret}}),$$

where $\overline{\theta}$ denotes the angular center of the aerosol region and Θ its angular half-width. The retrieval bounds are then given by $\theta_{\min}^{\text{ret}} = \overline{\theta} - \Theta$ and $\theta_{\max}^{\text{ret}} = \overline{\theta} + \Theta$.

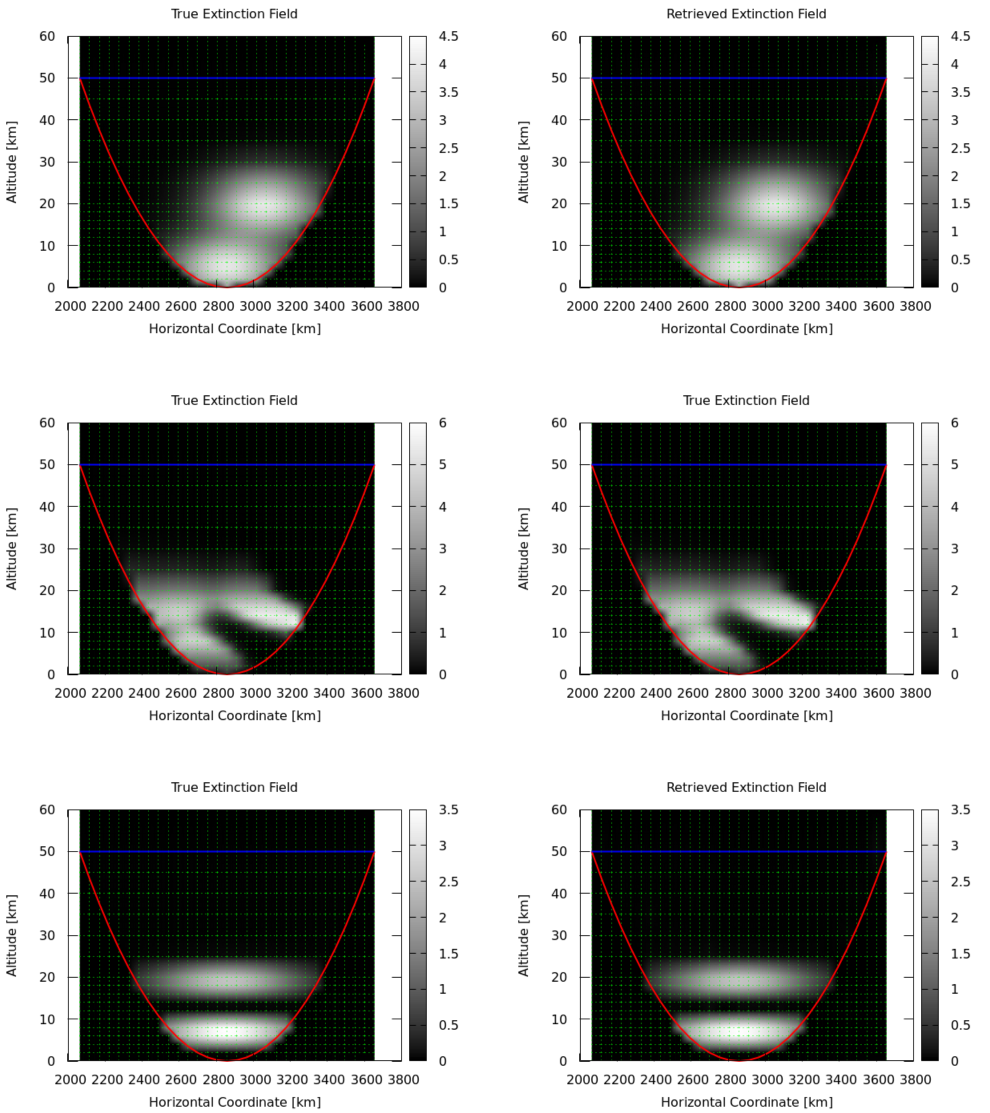

Figure 5. Verification of the unrestricted extinction-field retrieval in the idealized case where the synthetic measurements lie exactly in the range of the forward-model operator. (**Left column**) true extinction fields. (**Right column**) retrieved extinction fields. (**Top row**) two Gaussian extinction layers. (**Middle row**) cloud-like extinction structure. (**Bottom row**) two horizontally extended extinction layers. The inverse problem is solved using the multistart optimization algorithm described in Section 2.4.

The retrieved extinction field is modeled as a radially varying profile confined to a finite angular sector. Specifically, the extinction field is represented in the form

$$\sigma(R, \theta) = \sigma(R) B(\theta; \overline{\theta}, \Theta),$$

where $\sigma(R)$ describes the radial dependence of the extinction field and

$$B(\theta; \overline{\theta}, \Theta) = \frac{1}{2}\left[\tanh\left(\frac{\theta - \vartheta_{\min}}{\Delta\theta}\right) - \tanh\left(\frac{\theta - \vartheta_{\max}}{\Delta\theta}\right)\right],$$

with $\vartheta_{\min} = \overline{\theta} - \Theta$ and $\vartheta_{\max} = \overline{\theta} + \Theta$, is a smoothed box function describing the angular support of the aerosol layer. For sufficiently small values of the discretization step $\Delta\theta$, the function $B(\theta; \overline{\theta}, \Theta)$ approximates an ideal box profile equal to one inside the interval $[\overline{\theta} - \Theta, \overline{\theta} + \Theta]$ and approximately zero outside this region.

The unknown state vector $\mathbf{x}$ is formed by collecting the values of the radial extinction field, represented by the extinction vector

$$\boldsymbol{\sigma} = [\sigma(R_1), \sigma(R_2), \ldots, \sigma(R_{N_R})]^{\mathrm{T}},$$

together with the angular center of the aerosol region $\overline{\theta}$ and its angular half-width Θ, that is,

$$\mathbf{x} = \begin{bmatrix} \boldsymbol{\sigma} \\ \overline{\theta} \\ \Theta \end{bmatrix} \in \mathbb{R}^{N_{\mathrm{x}}},$$

where $N_{\mathrm{x}} = N_R + 2$. Thus, the retrieval simultaneously reconstructs both the radial extinction profile and the horizontal support of the aerosol field within the retrieval domain Ω.

Inverse Problem and Regularization

Let y_m^{δ} denote the measurement corresponding to limb ray m. Each limb ray is characterized by the tangent radius $R_{\mathrm{T}m}$, and let N_{y} denote the number of tangent radii, or equivalently, the number of limb rays. These tangent radii can be chosen as the radial grid points R_j, $j = 1, \ldots, N_R$, or obtained by subdividing each interval $[R_j, R_{j+1}]$ into a number of uniform subintervals. Then, for the forward model (15), we are led to the nonlinear equation

$$y_m^{\delta} = F(\sigma_{\mathrm{L}1}^{(m)}(\mathbf{x}), \ldots, \sigma_{\mathrm{L}N_m}^{(m)}(\mathbf{x})), \qquad m = 1, \ldots, N_{\mathrm{y}},$$

where N_m is the number of discretization points along ray m, and the limb-path extinction values $\sigma_{\mathrm{L}k}^{(m)}(\mathbf{x})$, $k = 1, \ldots, N_m$, are obtained by interpolation from the radial extinction values collected in $\boldsymbol{\sigma}$, combined with the angular support determined by the parameters $\overline{\theta}$ and Θ.

To stabilize the inversion, we introduce a first-order regularization term acting directly on the radial extinction profile $\sigma(R_j)$. The retrieval problem is then formulated as the minimization of the Tikhonov function

$$\mathcal{F}(\mathbf{x}) = \frac{1}{2}\left(\left\|\mathbf{F}(\mathbf{x}) - \mathbf{y}^{\delta}\right\|^2 + \alpha \left\|\mathsf{L}\mathbf{x}\right\|^2\right),$$

where

$$\mathcal{R}(\mathbf{x}) = \left\|\mathbf{F}(\mathbf{x}) - \mathbf{y}^{\delta}\right\|^2 = \sum_{m=1}^{N_{\mathrm{y}}} (F(\sigma_{\mathrm{L}1}^{(m)}(\mathbf{x}), \ldots, \sigma_{\mathrm{L}N_m}^{(m)}(\mathbf{x})) - y_m^{\delta})^2$$

is the square residual, α denotes the regularization parameter, and L is the regularization matrix. Specifically, the regularization matrix penalizes first-order radial variations of the extinction profile and is defined by

$$\mathsf{L} = [\mathsf{L}_{\sigma}, 0_{(N_R-1)\times 2}] \in \mathbb{R}^{(N_R-1)\times(N_R+2)},$$

where the nonzero components of $\mathsf{L}_{\sigma} \in \mathbb{R}^{(N_R-1)\times N_R}$ are

$$(\mathsf{L}_{\sigma})_{jj} = -\frac{1}{R_{j+1} - R_j}, \;\; (\mathsf{L}_{\sigma})_{j,j+1} = \frac{1}{R_{j+1} - R_j}, \;\; j = 1, \ldots, N_R - 1.$$

Thus, $\left\|\mathsf{L}\mathbf{x}\right\|^2 = \left\|\mathsf{L}_{\sigma}\boldsymbol{\sigma}\right\|^2$, showing that the regularization promotes smooth radial variations of the extinction field while leaving the angular support, described by the parameters $\overline{\theta}$ and Θ, unregularized.

Retrieval Constraints from AOT Observations

The objective function is minimized subject to simple bound constraints on the variables. Specifically, these are chosen as follows:

1. For the extinction field, we impose the lower and upper bounds σ_{low} and σ_{up}, respectively.
2. To constrain the horizontal extent of the extinction field, external aerosol optical thickness (AOT) observations are used. The use of nadir-view AOT information does not imply that the proposed GEO–LEO limb measurements have lower precision than nadir observations. Rather, the two measurement geometries provide complementary information about different characteristics of the aerosol field. Nadir AOT is a vertically integrated quantity that provides information about the horizontal occurrence and approximate horizontal extent of aerosol enhancements, but has only limited sensitivity to the vertical distribution of aerosol extinction. In contrast, GEO–LEO limb measurements are primarily sensitive to the radial, or vertical, distribution of the aerosol extinction field. Accordingly, the AOT product is used only to define relaxed bounds on the horizontal-support parameters; it is not used to prescribe either the extinction magnitude or its vertical profile.
3. Global aerosol optical thickness (AOT) products derived from satellite instruments such as MODIS, MISR, and TROPOMI are assumed to be available (see, e.g., Refs. [26–28]). In the present work, an effective horizontal footprint of approximately 10–20 km is assumed for these products. The two-dimensional AOT field $\tau_{\mathrm{AOT}}(\lambda, \varphi, t)$, where λ and φ denote longitude and latitude, respectively, is projected onto the horizontal coordinate θ of the GEO–LEO limb plane, yielding a one-dimensional projected AOT profile $T(\theta)$. In practice, this projection is performed by averaging AOT pixels within a finite cross-track corridor surrounding the atmospheric region sampled by the GEO–LEO limb rays. The corridor width is chosen according to the effective horizontal footprint of the AOT product. The projected AOT profile is then used as a proxy for the horizontal extent of the aerosol extinction field. Regions potentially containing enhanced aerosol loading are identified by the condition $T(\theta) > T_{\mathrm{HR}}$, where T_{HR} is determined from a background AOT level and its variability. This procedure yields the AOT-derived angular limits $\theta^{\mathrm{AOT}}_{\mathrm{min}}$ and $\theta^{\mathrm{AOT}}_{\mathrm{max}}$, as well as the corresponding estimates of the angular center and angular half-width,

$$\overline{\theta}_{\mathrm{AOT}} = \frac{1}{2}\left(\theta^{\mathrm{AOT}}_{\mathrm{max}} + \theta^{\mathrm{AOT}}_{\mathrm{min}}\right), \qquad \Theta_{\mathrm{AOT}} = \frac{1}{2}\left(\theta^{\mathrm{AOT}}_{\mathrm{max}} - \theta^{\mathrm{AOT}}_{\mathrm{min}}\right).$$

These quantities are subsequently used to define bounds for the retrieval parameters $(\overline{\theta}, \Theta)$. To account for the finite spatial footprint of the AOT products, retrieval smoothing, and the limited vertical discrimination inherent in AOT measurements, the bounds on the angular parameters are relaxed by introducing an uncertainty margin. In this work, we adopt

$$\delta\theta = \frac{20\,\mathrm{km}}{R_{\mathrm{Earth}}},$$

which corresponds to an angular uncertainty associated with a horizontal distance of approximately 20 km at the Earth's surface. This value is representative of the effective horizontal footprint of moderate-resolution AOT products and remains substantially smaller than the characteristic horizontal scales of the aerosol structures considered in this study. Accordingly, we impose the bounds

$$\overline{\theta}_{\mathrm{AOT}} - \delta\theta \leq \overline{\theta} \leq \overline{\theta}_{\mathrm{AOT}} + \delta\theta,$$

and

$$\max(\Theta_{\mathrm{AOT}} - \delta\theta, 0) \le \Theta \le \Theta_{\mathrm{AOT}} + \delta\theta.$$

To guarantee that the retrieved aerosol interval remains inside the geometrically admissible GEO–LEO retrieval domain, the AOT-derived angular limits are required to satisfy

$$\theta_{\min} + 2\delta\theta \le \theta_{\min}^{\mathrm{AOT}} < \theta_{\max}^{\mathrm{AOT}} \le \theta_{\max} - 2\delta\theta.$$

Under these assumptions, the retrieved aerosol interval satisfies $\theta_{\min} \le \theta_{\min}^{\mathrm{ret}} < \theta_{\max}^{\mathrm{ret}} \le \theta_{\max}$. For sufficiently large values of Θ_{AOT}, the admissible intervals for $\overline{\theta}$ and Θ have widths approximately equal to $2\delta\theta$. This corresponds to an uncertainty of about ± 20 km in the horizontal localization of the aerosol boundaries, or approximately 40 km for the total admissible interval.

Alternative Regularization

In principle, the variables $\overline{\theta}$ and Θ can also be regularized by considering the constraint term

$$\mathcal{C}(\mathbf{x}) = \left\| \mathsf{L}_\sigma \boldsymbol{\sigma} \right\|^2 + w_\theta[(\overline{\theta} - \overline{\theta}_{\mathrm{AOT}})^2 + (\Theta - \Theta_{\mathrm{AOT}})^2],$$

where w_θ is a weighting factor, $\overline{\theta}_{\mathrm{AOT}} = (\theta_{\max}^{\mathrm{AOT}} + \theta_{\min}^{\mathrm{AOT}})/2$,and $\Theta_{\mathrm{AOT}} = (\theta_{\max}^{\mathrm{AOT}} - \theta_{\min}^{\mathrm{AOT}})/2$. However, since $\overline{\theta}_{\mathrm{AOT}}$ and Θ_{AOT} are not known precisely, we prefer to use this information only to impose bounds on $\overline{\theta}$ and Θ. In this sense, simple bound constraints on the variables may also be regarded as a form of regularization.

2.3.2. Parametric Extinction Retrieval

In this section, we develop a parametric formulation of the aerosol extinction retrieval. The extinction field is represented as a combination of physically motivated components describing the dominant aerosol structures, and the corresponding inverse problem is formulated in terms of a small set of model parameters. The advantages and limitations of the proposed approach are also discussed.

Parametric Model

We express the two-dimensional aerosol extinction field as $\sigma = \sigma(h, \theta)$, where, $h = R - R_{\mathrm{Earth}}$ denotes the altitude above the Earth's surface. The extinction field is approximated by means of a nonlinear parametric model constructed from a small number of physically motivated building blocks. The corresponding parameter vector is denoted by

$$\boldsymbol{\eta} = [\eta_1, \eta_2, \ldots, \eta_{N_{\mathrm{par}}}]^{\mathrm{T}},$$

where N_{par} is the number of parameters. The model is designed to capture typical aerosol structures observed in the upper troposphere and lower stratosphere, such as background extinction, elevated aerosol layers, and transported plumes.

The parametric representation is based on the following elementary functions.

1. Exponential background. The large-scale background extinction is modeled by an exponentially decaying profile,

$$\sigma_{\mathrm{bg}}(h; \boldsymbol{\eta}_{\mathrm{bg}}) = A_{\mathrm{bg}} \exp\left(-\frac{h}{h_{\mathrm{bg}}}\right),$$

where $A_{\mathrm{bg}} > 0$ is the amplitude, $h_{\mathrm{bg}} > 0$ is the scale height, and $\boldsymbol{\eta}_{\mathrm{bg}} = [A_{\mathrm{bg}}, h_{\mathrm{bg}}]^{\mathrm{T}}$.

2. Gaussian functions. Localized aerosol layers are described using Gaussian functions of the form
$$G(u; u_0, \varsigma) = \exp\left(-\frac{(u-u_0)^2}{2\varsigma^2}\right), \qquad \varsigma > 0,$$
where u_0 is the center and ς is the standard deviation. In particular, we use vertical Gaussians $G(h; h_0, \varsigma_h)$ and angular Gaussians $G(\theta; \theta_0, \varsigma_\theta)$.
3. Smoothed box layers. Layered structures are modeled using smoothed box functions,
$$B(h; h_b, h_t, w_b) = \frac{1}{2}\left[\tanh\left(\frac{h-h_b}{w_b}\right) - \tanh\left(\frac{h-h_t}{w_b}\right)\right],$$
where h_b and h_t denote the lower and upper boundaries of the layer, and $w_b > 0$ controls the smoothness of the transitions.

To represent realistic atmospheric scenarios, we introduce the following basic components.

1. Elevated aerosol layer. Localized elevated aerosol layers are modeled by
$$\sigma_{\mathrm{EL}}(h, \theta; \boldsymbol{\eta}_{\mathrm{EL}}) = A_{\mathrm{EL}}\, G(h; h_{\mathrm{EL}}, \varsigma_{h,\mathrm{EL}})[1 + A_{\mathrm{rel,EL}}\, G(\theta; \theta_{\mathrm{EL}}, \varsigma_{\theta,\mathrm{EL}})],$$
where $\boldsymbol{\eta}_{\mathrm{EL}} = [A_{\mathrm{EL}}, h_{\mathrm{EL}}, \varsigma_{h,\mathrm{EL}}, A_{\mathrm{rel,EL}}, \theta_{\mathrm{EL}}, \varsigma_{\theta,\mathrm{EL}}]^{\mathrm{T}}$.
2. Broad stratospheric aerosol layer. Broad stratospheric aerosol layers are used to approximate volcanic or smoke layers that extend over several kilometers in altitude and may cover large geographical regions. They are modeled by
$$\sigma_{\mathrm{LS}}(h, \theta; \boldsymbol{\eta}_{\mathrm{LS}}) = A_{\mathrm{LS}}\, B(h; h_b, h_t, w_b)[1 + A_{\mathrm{rel,LS}}\, G(\theta; \theta_{\mathrm{LS}}, \varsigma_{\theta,\mathrm{LS}})],$$
where $\boldsymbol{\eta}_{\mathrm{LS}} = [A_{\mathrm{LS}}, h_b, h_t, w_b, A_{\mathrm{rel,LS}}, \theta_{\mathrm{LS}}, \varsigma_{\theta,\mathrm{LS}}]^{\mathrm{T}}$.
3. Tilted plume. Transported aerosol plumes with vertical tilt are modeled by
$$\sigma_{\mathrm{PL}}(h, \theta; \boldsymbol{\eta}_{\mathrm{PL}}) = A_{\mathrm{PL}}\, G(h; h_{\mathrm{PL}}, \varsigma_{h,\mathrm{PL}})\, G(\theta; \theta_{\mathrm{PL},0} + s_{\mathrm{PL}}(h - h_{\mathrm{PL}}), \varsigma_{\theta,\mathrm{PL}}),$$
where $\boldsymbol{\eta}_{\mathrm{PL}} = [A_{\mathrm{PL}}, h_{\mathrm{PL}}, \varsigma_{h,\mathrm{PL}}, \theta_{\mathrm{PL},0}, s_{\mathrm{PL}}, \varsigma_{\theta,\mathrm{PL}}]^{\mathrm{T}}$.

Combining all contributions, the extinction field is expressed as
$$\sigma(h, \theta; \boldsymbol{\eta}) = \sigma_{\mathrm{bg}}(h; \boldsymbol{\eta}_{\mathrm{bg}}) + \sigma_{\mathrm{EL}}(h, \theta; \boldsymbol{\eta}_{\mathrm{EL}}) + \sigma_{\mathrm{LS}}(h, \theta; \boldsymbol{\eta}_{\mathrm{LS}}) + \sigma_{\mathrm{PL}}(h, \theta; \boldsymbol{\eta}_{\mathrm{PL}}).$$

For this representation, the number of unknown parameters is $N_{\mathrm{par}} = 21$. The effective horizontal extent and localization of the aerosol structures are determined by the angular Gaussian functions $G(\theta; \theta_0, \varsigma_\theta)$, whose centers and widths are treated as retrieval parameters.

Inverse Formulation

The objective function to be minimized is
$$\mathcal{F}(\boldsymbol{\eta}) = \frac{1}{2}[\|\mathbf{F}(\boldsymbol{\eta}) - \mathbf{y}^\delta\|^2 + \alpha\|\mathsf{L}(\boldsymbol{\eta} - \boldsymbol{\eta}_{\mathrm{a}})\|^2],$$
that is
$$\mathcal{F}(\boldsymbol{\eta}) = \frac{1}{2}\left[\sum_{m=1}^{N_{\mathrm{y}}} (F(\sigma_{\mathrm{L1}}^{(m)}(\boldsymbol{\eta}), \ldots, \sigma_{\mathrm{L}N_m}^{(m)}(\boldsymbol{\eta})) - y_m^\delta)^2 + \alpha\|\mathsf{L}(\boldsymbol{\eta} - \boldsymbol{\eta}_{\mathrm{a}})\|^2\right],$$
where L is a diagonal regularization matrix and $\boldsymbol{\eta}_{\mathrm{a}}$ is the a priori state vector.

Discussion

In summary, the proposed parametric representation combines a small number of physically interpretable components to describe the dominant large-scale stratospheric aerosol structures, including background extinction, elevated aerosol layers, broad stratospheric layers, and transported plumes. The resulting model is flexible yet low-dimensional, making it well suited for nonlinear inversion and parameter estimation. Unlike the radial-grid retrieval, which makes only weak assumptions regarding the aerosol morphology and is therefore applicable to arbitrary extinction fields, the parametric formulation is intended for situations in which the dominant aerosol distribution can be represented by the adopted model class. By substantially reducing the number of unknowns, the parametric approach improves the conditioning of the inverse problem, requires less regularization, and generally yields more stable and robust retrievals.

The objective of the parameterized retrieval is not to reproduce the full spatial complexity of the aerosol extinction field, but rather to recover its dominant physically meaningful characteristics. Consequently, when the true aerosol distribution lies outside the assumed model class, the retrieved solution represents the best approximation in the least-squares sense. Fine-scale structures, irregular features, and multimodal distributions may therefore be absorbed into broader components, resulting in a stable but approximate reconstruction. In contrast, the radial-grid formulation is better suited to such complex aerosol fields, although at the expense of a substantially larger number of unknowns and a more severely ill-conditioned inverse problem.

2.4. Multistart Optimization Algorithm

The inverse problem is solved using a multistart optimization strategy specifically designed for nonlinear ill-posed problems [29,30]. The algorithm combines global exploration of the admissible parameter space with local optimization, discrepancy-principle filtering, and clustering of acceptable solutions. The main steps for minimizing the objective function $\mathcal{F}(\mathbf{x})$ (or $\mathcal{F}(\boldsymbol{\eta})$ in the case of parametric extinction retrieval) are summarized as follows.

1. *Main input parameters.* The relevant input parameters of the algorithm are the number of configurations N_{conf}, the number of random candidate starting points N_{start}, the number of retained starting points N_{start0}, the lower and upper bounds on the state vector $\mathbf{x}_{\mathrm{low}}$ and $\mathbf{x}_{\mathrm{up}}$, the noise level Δ, and a relative distance tolerance $\varepsilon_{\mathrm{clst}}$ used to determine the number of clusters.
2. *Initialization*. The algorithm initializes the best residual, the best reconstruction error, and the best cluster-center solution.
3. *Generation of candidate starting points.* For each configuration, a large number of random parameter vectors $\mathbf{x}_0^{(i)}$, $i = 1, \ldots, N_{\mathrm{start}}$ is generated within the admissible bounds of $\mathbf{x}$.
4. *Evaluation of the objective function.* For each candidate vector $\mathbf{x}_0^{(i)}$, the residual function $\mathcal{R}(\mathbf{x}_0^{(i)})$ is evaluated and stored.
5. *Sorting of the candidates.* The candidate starting points are sorted in increasing order of their residual-function values. Consequently, the most promising candidates are placed first.
6. *Selection of a reduced starting set.* From the sorted candidate set, only N_{start0} starting points are retained. This selection can be performed by distance filtering, importance sampling, hybrid selection, stochastic optimization algorithms, or simply by retaining the best-ranked candidates.
7. *Loop over the retained starting points.* A loop over the retained starting points is performed.
   (a) *Validation check.* Each starting point is checked for validity and admissibility with respect to the imposed constraints and parameter bounds. Possible

validation tests include the function-distance test, the basin-exclusion test, and the gradient-distance test; their definitions are given in Appendix C.

(b) *Local search.* If the starting point is admissible, a local bounded optimization procedure is performed. The output includes the final local minimizer, its residual value, the radius of its basin of attraction, and several intermediate solutions satisfying the discrepancy principle. The precise discrepancy interval based on the noise level Δ is defined in Appendix C.

(c) *Collection of discrepancy-principle solutions.* All discrepancy-principle solutions returned by the local optimization are stored in an array, provided that they are not duplicates of previously detected solutions. If a newly obtained solution is sufficiently close to an existing one, only the solution with the smaller residual is retained.

(d) *Clustering of accepted solutions.* The accepted solutions are clustered in parameter space using a single-linkage (distance-based) criterion with relative distance tolerance $\varepsilon_{\mathrm{clst}}$. For each cluster, a representative center is computed and its residual value is evaluated.

(e) *Tracking the minimum-error solution.* When the algorithm is tested using synthetic data with known exact solution, the solution with the smallest relative error with respect to the exact solution is recorded. This quantity is used only for diagnostic and validation purposes.

(f) *Tracking the minimum-residual solution.* Independently of the exact solution, the algorithm stores the solution with the smallest residual value found so far.

(g) *Tracking the minimum-cluster solution.* Among the cluster centers, the algorithm retains the one with the smallest residual. This solution represents a stable representative of a group of similar acceptable reconstructions.

8. *Stopping over configurations.* After each configuration, i.e., after completing the loop over the retained starting points, the algorithm checks whether the current best residual is sufficiently small. If this condition is satisfied, the loop over configurations is terminated. Otherwise, an additional configuration may be tested, provided that the total number of configurations remains below the prescribed maximum value N_{conf}. The algorithm terminates when either the residual criterion is satisfied or the number of tested configurations reaches N_{conf}.
9. *Outputs*. The principal outputs are the minimum-error solution, when the exact solution is known, and the minimum-cluster solution. The minimum-residual solution is retained as an additional diagnostic. Residual values and information-content measures, including averaging kernels, degrees of freedom, and condition numbers of the regularized Hessian, are subsequently computed for the selected solutions as described in Appendix C.

Appendix C provides the mathematical definitions and implementation details of the candidate-generation and selection strategies, validation tests, local optimization methods, discrepancy-principle filtering, regularization-parameter selection, and information-content diagnostics.

3. Numerical Simulations

In this section, we present numerical results for the two retrieval strategies considered in the present study.

3.1. Synthetic-Data Generation and Simulation Setup

This section describes the generation of the synthetic measurement data and the numerical setup used in the retrieval experiments. It includes the observation geometry, discretization, retrieval bounds, and the multistart and regularization settings adopted in the simulations.

3.1.1. Generation of the Synthetic Measurements

The synthetic measurement vector is generated in several steps in order to account for both measurement noise and systematic forward-model errors. First, for a specified exact (true) solution $\mathbf{x}^{\dagger}$, the exact data vector is computed from the forward model, $\mathbf{y} = \mathbf{F}(\mathbf{x}^{\dagger})$. As already discussed in Section 2.2, the possible influence of multiple scattering and other systematic modeling errors is represented by a conservative uniform perturbation of the synthetic data. Accordingly, the unperturbed data are scaled according to $\mathbf{y}^{\mathrm{fm}} = 1.1\,\mathbf{y}$. This corresponds to a uniform 10% perturbation of all components of the data vector and is deliberately larger than the approximately 6% error due to neglecting multiple scattering estimated in Ref. [23]. Finally, additive Gaussian noise is added to the biased forward model: $\mathbf{y}^{\delta} = \mathbf{y}^{\mathrm{fm}} + \delta$, where $\delta \sim \mathcal{N}(0, \mathsf{C}_{\delta})$ denotes the measurement noise, $\mathsf{C}_{\delta} = \sigma^2 \mathsf{I}$ is the corresponding noise covariance matrix, and I denotes the identity matrix. The noise variance σ^2 is chosen according to a prescribed signal-to-noise ratio (SNR) as $\sigma^2 = \|\mathbf{y}\|^2 / (N_{\mathrm{y}}\,\mathrm{SNR})$, so that $\mathbb{E}\{\|\delta\|^2\} = \|\mathbf{y}\|^2/\mathrm{SNR}$. The resulting vector $\mathbf{y}^{\delta}$ is used as the synthetic measurement vector in the inversion procedure. The corresponding squared perturbation level is estimated by $\Delta^2 = \|\mathbf{F}(\mathbf{x}^{\dagger}) - \mathbf{y}^{\delta}\|^2$which measures the discrepancy between the exact forward model and the noisy biased measurements. Since $\mathbf{y}^{\delta}$ contains both additive random noise and systematic forward-model errors, Δ^2 represents a combined perturbation level rather than purely stochastic measurement noise.

3.1.2. Scope of the Numerical Simulations

The synthetic measurements are intended to reproduce the dominant physical characteristics of GEO–LEO inter-satellite laser-link observations while maintaining a controlled environment for assessing the retrieval algorithm. Accordingly, the simulations incorporate the actual observation geometry, nonlinear radiative transfer, measurement noise, and systematic forward-model errors. However, several instrument- and mission-specific effects, such as laser power fluctuations, detector calibration uncertainties, pointing errors, timing uncertainties, background solar radiation, and orbital navigation errors, are not included explicitly. The present numerical experiments should therefore be regarded as proof-of-concept simulations designed to evaluate the mathematical formulation and inversion methodology rather than to reproduce all aspects of a specific future mission. A comprehensive end-to-end instrument simulation is left for future work.

3.1.3. Observation Geometry, Discretization, and Retrieval Bounds

In the simulations we consider an uniform radial grid between $R_{\mathrm{Tmin}} = 8$ km and $R_{\mathrm{Tmax}} = 28$ km with a grid spacing of $\Delta R = 1$ km. Thus, the number of radial grid points R_j is $N_R = 21$. The tangent radii $R_{\mathrm{T}j}$ are chosen to coincide with the radial grid points R_j. Consequently, the number of limb rays is $N_{\mathrm{y}} = 21$. For a GEO orbital radius $R_{\mathrm{G}} = R_{\mathrm{Earth}} + 35{,}786$ km, a LEO orbital radius $R_{\mathrm{L}} = R_{\mathrm{Earth}} + 500$ km, and the chosen radial grid, the angular boundaries of the retrieval domain are $\theta_{\min} = 76.76^{\circ}$ and $\theta_{\max} = 85.81^{\circ}$. The angular interval $[\theta_{\min}, \theta_{\max}]$ is discretized using $N_{\theta} = 91$ grid points. The AOT angular limits are chosen as $\theta_{\min}^{\mathrm{AOT}} = 81.11^{\circ}$ and $\theta_{\max}^{\mathrm{AOT}} = 83.26^{\circ}$, yielding $\overline{\theta}_{\mathrm{AOT}} = 82.19^{\circ}$ and $\Theta_{\mathrm{AOT}} = 1.08$. For these values of $\overline{\theta}_{\mathrm{AOT}}$ and Θ_{AOT}, and with the uncertainty margin $\delta\theta = 20\,\mathrm{km}/R_{\mathrm{Earth}}$, the bound intervals imposed on $\overline{\theta}$ and Θ are $[82.01^{\circ}, 82.36^{\circ}]$ and

$[0.90, 1.26]$, respectively. To generate the exact data vector, we adopt the values $\overline{\theta}^{\dagger} = \overline{\theta}_{\mathrm{AOT}}$ and $\Theta^{\dagger} = \Theta_{\mathrm{AOT}}$. For the extinction field, the lower and upper bounds are chosen as $\sigma_{\mathrm{low}} = 10^{-5}\,\mathrm{km}^{-1}$ and $\sigma_{\mathrm{up}} = 4 \times 10^{-3}\,\mathrm{km}^{-1}$, respectively.

3.1.4. Multistart and Regularization Settings

The multistart algorithm is used with the following parameters: the number of configurations $N_{\mathrm{conf}} = 1$, the number of random candidate starting points $N_{\mathrm{start}} = 15{,}000$, the number of retained starting points $N_{\mathrm{start0}} = 50$, and the relative cluster-distance tolerance $\varepsilon_{\mathrm{clst}} = 10^{-2}$. Candidate starting points are generated using a Faure sequence, the distance-filter strategy is employed to select a reduced set of starting points, the basin-exclusion test is used as the validation criterion, and the PORT routine is employed as the local bounded optimization method (Appendix C). The optimal value of the regularization parameter α_{opt} is determined by considering a logarithmically spaced set of values in the interval $10^{-3} \leq \alpha \leq 10^{4}$, with successive values differing by one order of magnitude.

3.2. Retrieval Results for Radial-Grid Extinction Values

Figures 6–9 and Table 2 present retrieval results for several synthetic aerosol test scenarios. The first scenario exhibits a vertically structured aerosol layer with multiple local features in the extinction profile, the second scenario corresponds to a smoother and more monotonic aerosol distribution, the third scenario contains a broad aerosol layer centered near the middle atmosphere, the fourth scenario shows a relatively narrow low-altitude aerosol structure, the fifth and sixth scenarios demonstrate correspond to aerosol layers with different vertical widths and amplitudes, and finally, the seventh scenario again contains a narrow structured aerosol layer with a pronounced extinction maximum. Each scenario includes the synthetic two-dimensional aerosol extinction field, the comparison between the true and retrieved (minimum-cluster solution) vertical extinction profiles $\boldsymbol{\sigma}^{\dagger}$ and $\boldsymbol{\sigma}_{\mathrm{C}}$, and the comparison between the measured, the biased, and the reconstructed limb radiances $\mathbf{y}^{\delta}$, $\mathbf{y}^{\mathrm{fm}}$, and $\mathbf{F}(\mathbf{x}_{\mathrm{C}})$, respectively. Table 2 summarizes the corresponding quantitative retrieval errors, including the relative extinction error ε_{σ}, the absolute error in the angular center $\epsilon_{\overline{\theta}}$, the relative error in the angular half-width ε_{Θ}, the relative measurement residual $\varepsilon_{\mathrm{y}} = \|\mathbf{y}^{\mathrm{fm}} - \mathbf{F}(\mathbf{x}_{\mathrm{C}})\| / \|\mathbf{y}^{\mathrm{fm}}\|$, the effective degrees of freedom DoF, and the condition number of the regularized Hessian $\kappa(\mathsf{H})$. The relative extinction error represents the relative root-mean-square error between the exact and retrieved extinction fields evaluated at the radial and angular grid points. The following conclusions may be drawn:

1. Overall, the retrieved extinction profiles reproduce the main aerosol structures with good accuracy. The altitude, amplitude, and vertical extent of the aerosol layers are recovered reliably in most scenarios. The corresponding extinction errors remain moderate, typically between approximately 5% and 12%. The retrieval quality depends on the structure of the aerosol layer. Smooth and vertically broad layers are reconstructed more accurately than narrow or sharply localized structures. The largest discrepancies occur for low-altitude aerosol layers (Scenario 4), where the sensitivity of the limb measurements decreases and the inverse problem becomes more ill-conditioned.
2. The retrieval of the angular center is particularly accurate. The absolute angular errors $\epsilon_{\overline{\theta}}$ remain below 0.08° in all cases and are frequently much smaller. Even the largest error of 0.08° corresponds to a horizontal displacement of approximately 8.9 km along the Earth's surface, which is smaller than the adopted uncertainty margin of 20 km.
3. The relative errors in the angular half-width, ε_{Θ}, are larger than the angular-center errors, but still remain moderate. Most values lie between approximately 3% and 9%. This behavior is expected, because the reconstruction of the plume width is generally more difficult than the reconstruction of its center location. The limb measurements

are most sensitive near the tangent region, which strongly constrains the plume position, whereas the plume boundaries influence the measurements more weakly and therefore are reconstructed with lower accuracy. Nevertheless, the retrieved horizontal extents remain reasonably close to the true values in all scenarios.

4. The measurement residuals ε_{y} are small, generally between approximately 2% and 5%. This indicates that the reconstructed extinction fields reproduce the measured limb radiances well. In particular, several scenarios yield residuals below 2%, demonstrating a high level of consistency between the forward model and the retrieved solution. Scenario 4 produces the largest residuals, which also coincides with the largest extinction reconstruction errors. This suggests that Scenario 4 is intrinsically more difficult, likely because of reduced sensitivity, stronger nonlinearity, or increased ambiguity in the retrieval geometry.
5. The effective degrees of freedom provide important information about the amount of independent information contained in the retrieval. The degrees of freedom range from approximately 10 to 16.5. This means that the measurements effectively determine only about 10–16 independent combinations of the 21 unknown parameters. In particular, DoF $\approx$ 16 indicates a relatively informative retrieval, with most of the vertical structures being constrained by the measurements, whereas DoF $\approx$ 10 indicates stronger smoothing and a lower effective vertical resolution.
6. The condition numbers of the regularized Hessian remain on the order of 10^6, confirming that the inverse problem remains strongly ill-conditioned even after regularization. However, despite this severe ill-conditioning, the retrieval errors remain moderate and stable. This demonstrates the effectiveness of the combined inversion strategy based on Tikhonov regularization, discrepancy-based solution filtering, multistart optimization, and clustering of admissible solutions. The results suggest that the proposed methodology stabilizes the inversion sufficiently to obtain physically meaningful aerosol reconstructions even in the presence of multiple local minima and limited angular information. Another important observation is that a smaller condition number does not necessarily imply a smaller reconstruction error. For example, Scenario 4 has a relatively small condition number compared with the other scenarios, 1.17×10^6, yet exhibits the largest extinction error, 12.46%. This illustrates that the retrieval accuracy is not determined solely by numerical conditioning, but also by the measurement sensitivity, the geometry, the effective degrees of freedom, and the structure of the aerosol extinction field itself. In nonlinear inverse problems, the relationship between conditioning and reconstruction quality is therefore not always monotonic.

Table 2. Retrieval results for the scenarios shown in Figures 6–9.

Scenario	ε_σ**[%]**	$\epsilon_{\overline{\theta}}$**[deg]**	ε_Θ**[%]**	ε_{y}**[%]**	**DoF**	$\kappa(\mathbf{H})$
1	8.38	0.08	9.28	2.46	16.50	3.46×10^6
2	5.99	0.08	3.62	2.34	16.23	1.74×10^6
3	5.14	0.02	8.44	1.85	14.93	1.09×10^6
4	12.46	0.07	7.70	5.50	10.20	1.17×10^6
5	6.03	0.01	6.12	2.08	15.73	1.05×10^6
6	8.98	0.06	3.15	2.49	14.26	1.37×10^6
7	6.26	0.04	8.95	1.86	10.03	1.21×10^6

https://doi.org/10.3390/atmos17080737

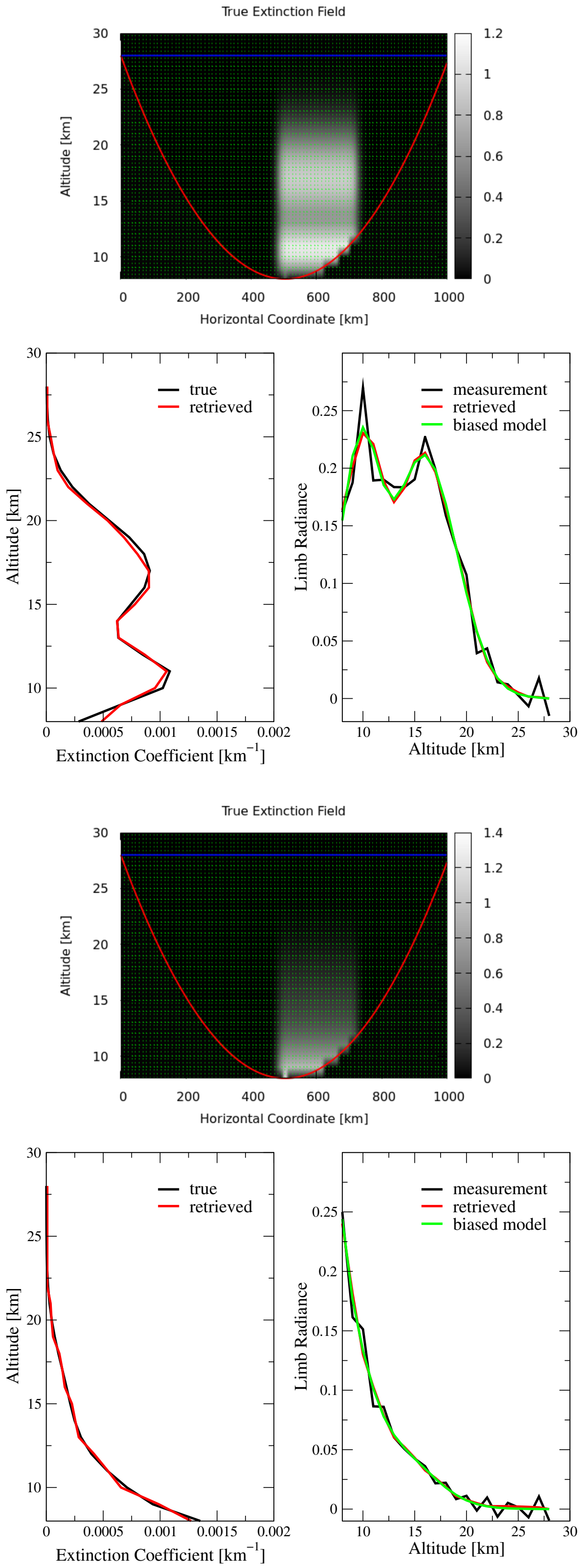

Figure 6. Aerosol extinction retrievals for Scenarios 1 and 2: a vertically structured multilayer profile and a smooth monotonically decreasing profile. The extinction coefficients are scaled by 10^3 km^{-1}.

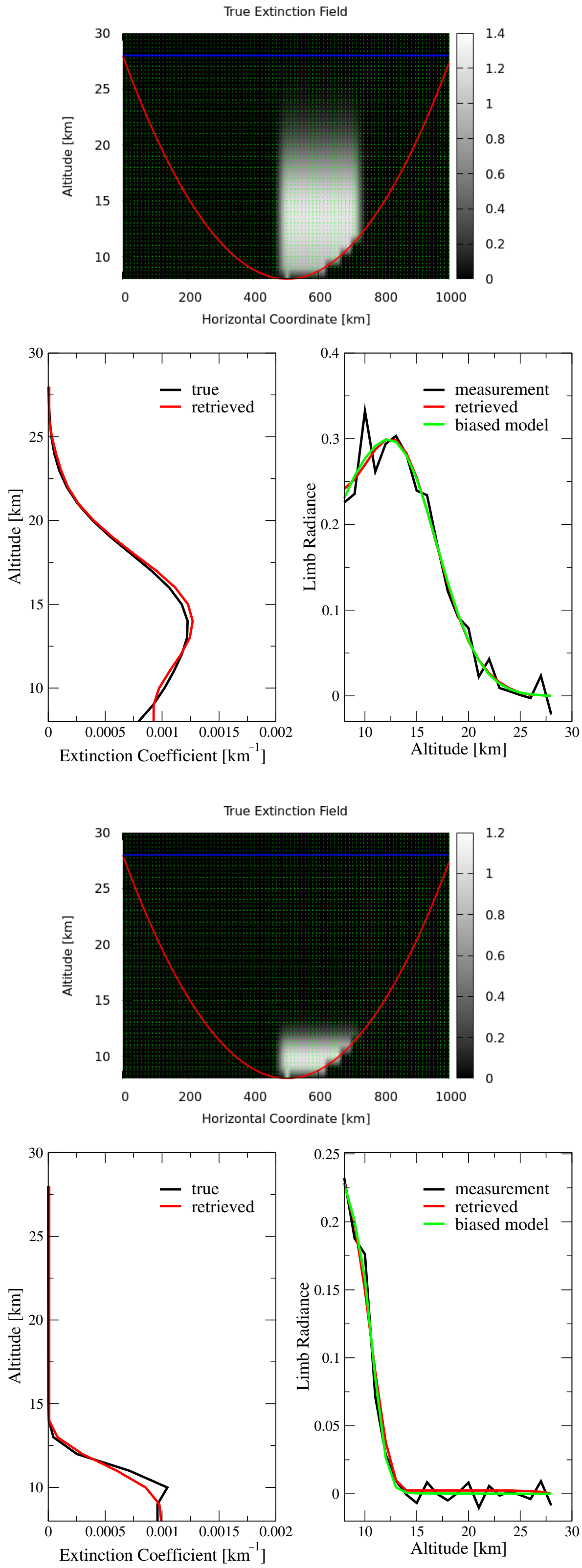

Figure 7. Aerosol extinction retrievals for Scenarios 3 and 4: a broad middle-atmospheric aerosol layer and a narrow low-altitude layer. The extinction coefficients are scaled by 10^3 km^{-1}.

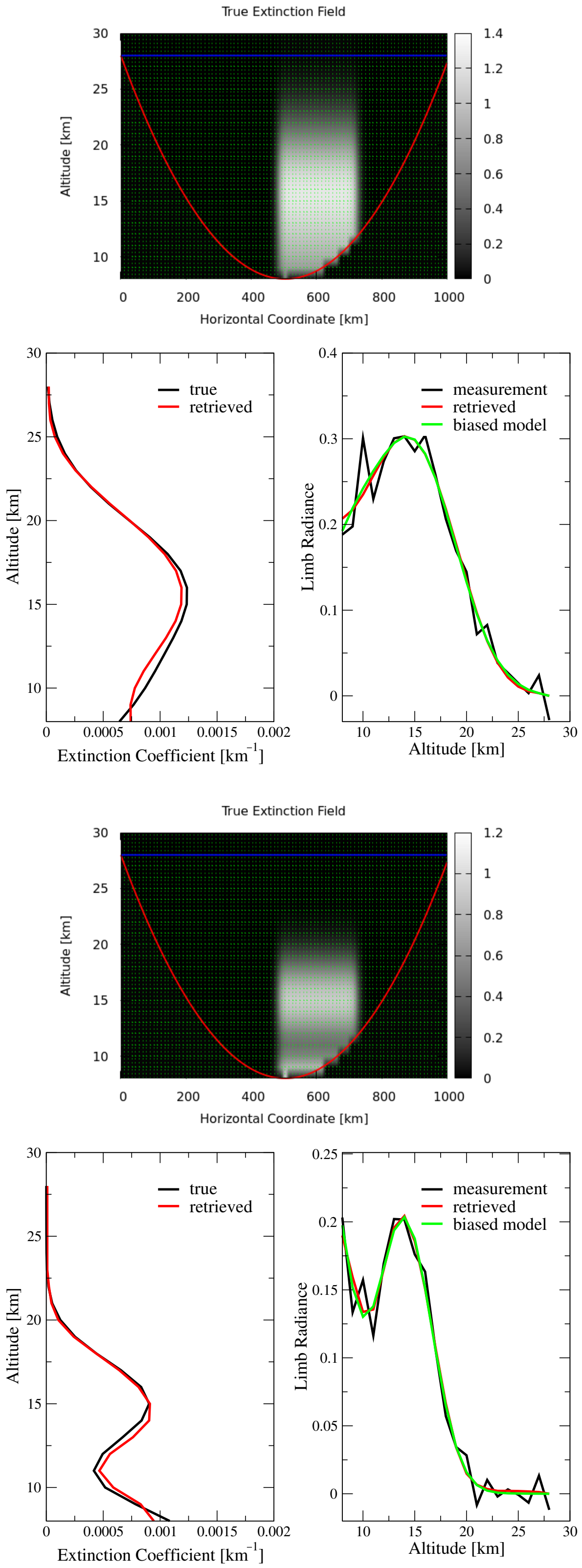

Figure 8. Aerosol extinction retrievals for Scenarios 5 and 6: aerosol layers with different vertical widths and amplitudes. The extinction coefficients are scaled by 10^3 km^{-1}.

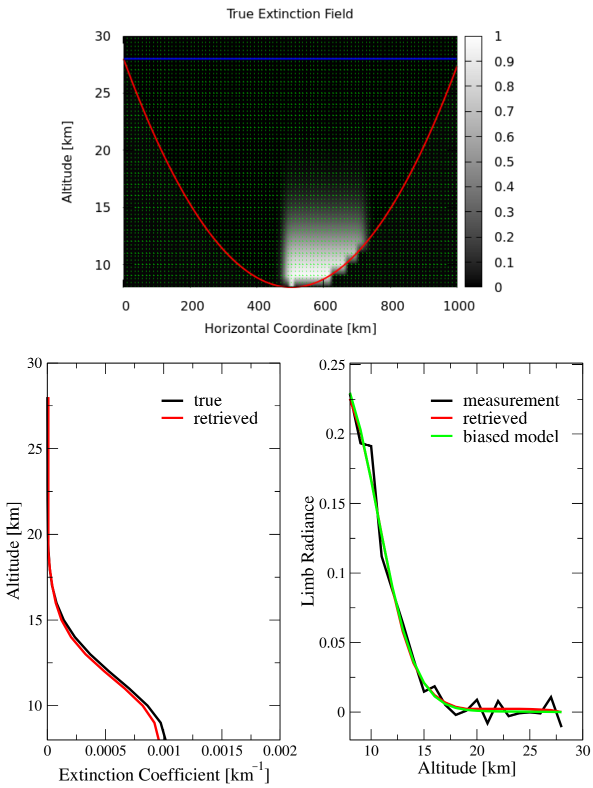

Figure 9. Aerosol extinction retrievals for Scenario 7: a narrow structured layer with a pronounced extinction maximum. The extinction coefficients are scaled by 10^3 km^{-1}.

3.3. Retrieval Results for Parameterized Extinction Fields

In contrast to the previous retrieval strategy, in which the extinction field was reconstructed directly from the radial grid values, the present approach represents the aerosol distribution by means of a set of parameters describing the dominant geometric characteristics of the aerosol structures. Consequently, the state vector consists of the model parameters and has dimension $N_{\mathrm{par}} = 21$. The measurement vector, the radial and angular grids, and the retrieval domain are generated as in the previous example. However, in the present case, the number of limb rays is $N_{\mathrm{y}} = 41$, meaning that each interval $[R_j, R_{j+1}]$ is divided into two equal subintervals.

Figures 10–12 and Table 3 present retrieval results for several synthetic aerosol test scenarios using a parametric representation of the aerosol extinction field. The first scenario corresponds to a vertically broad aerosol plume with both lower and elevated extinction structures, the second scenario contains a smoother and more compact lower-stratospheric aerosol layer, the third scenario represents a broad vertically elongated aerosol distribution extending toward higher altitudes, the fourth scenario exhibits a compact isolated elevated plume centered near the middle atmosphere, the fifth scenario corresponds to a shallow low-altitude aerosol layer with rapidly decreasing extinction, and the sixth scenario contains a broad and horizontally broad aerosol layer occupying a large portion of the retrieval domain. The figures compare the true and retrieved extinction fields for different synthetic aerosol scenarios, while Table 3 summarizes the corresponding quantitative retrieval errors, including the relative extinction error ε_σ, the relative measurement residual ε_{y}, the effective degrees of freedom DoF, and the condition number of the regularized Hessian $\kappa(\mathsf{H})$. Several conclusions can be drawn from these results:

1. Overall, the retrieved extinction fields reproduce the main morphology of the aerosol structures with good accuracy. The reconstructed plumes preserve the dominant

vertical and horizontal localization characteristics of the true aerosol extinction fields while remaining spatially smooth and physically consistent. Moderate smoothing effects are visible near plume boundaries, but no significant oscillatory artifacts appear in the reconstructions.

2. The radiance residuals remain extremely small in all scenarios, typically below approximately 0.35%, whereas the extinction errors remain moderate, generally between approximately 6% and 10%. The figures further indicate that the parametric representation is particularly well suited for smooth and compact aerosol structures. The reconstructed plumes retain the approximate Gaussian-like shapes, smooth boundaries, and central locations of the true aerosol extinction fields. Since the synthetic test cases are themselves relatively smooth, the parametric model provides a good representation of the true aerosol morphology, thereby explaining the small residuals and the overall accuracy of the reconstructions.
3. The effective degrees of freedom remain relatively large, ranging approximately between 10 and 18. This indicates that the measurements still contain substantial independent information about the aerosol extinction field and that the improved conditioning is not achieved through a loss of retrievable information.
4. The condition number is substantially reduced compared with the previous grid-based retrieval strategy. Whereas the direct reconstruction of radial extinction values yielded condition numbers on the order of 10^6, the parametric representation reduces these values to approximately $6 \times 10^4 - 3 \times 10^5$. Although the number of unknowns remains the same in both approaches, the parameterized representation introduces stronger structural correlations between neighboring regions of the extinction field. Consequently, the admissible solution space becomes more closely aligned with smooth and physically plausible aerosol structures supported by the measurements, thereby suppressing weakly observable and highly oscillatory solution components.

Compared with the direct grid-based retrieval strategy, the parameterized approach improves the conditioning of the inverse problem, suppresses oscillatory artifacts, and yields highly accurate radiance fits while preserving the dominant physical characteristics of the aerosol extinction field. It should be emphasized, however, that the favorable retrieval results obtained in the present simulations are partly due to the fact that the synthetic extinction fields were generated using the same parametric representation as that employed in the inversion. Consequently, the true aerosol distributions belong to the assumed model class, allowing the retrieval algorithm to reproduce the dominant aerosol structures with high accuracy. The more general problem of retrieving arbitrary aerosol extinction fields that do not belong to the assumed parametric model class is not considered in the present study. In realistic applications, deviations between the true aerosol distribution and the adopted parameterization may lead to larger reconstruction errors and stronger smoothing effects. As discussed previously, the simplified parameterization is intended primarily to capture the dominant observable features of the aerosol extinction field rather than its full spatial complexity.

Table 3. Retrieval results for the scenarios shown in Figures 10 and 12.

Scenario	ε_σ[%]	ε_y[%]	DoF	$\kappa(\mathbf{H})$
1	7.67	0.34	17.78	7.46×10^4
2	6.14	0.31	15.56	7.52×10^4
3	10.01	0.23	10.45	3.09×10^5
4	9.38	0.33	14.36	1.17×10^5
5	7.69	0.32	17.41	8.03×10^4
6	6.38	0.31	15.17	6.42×10^4

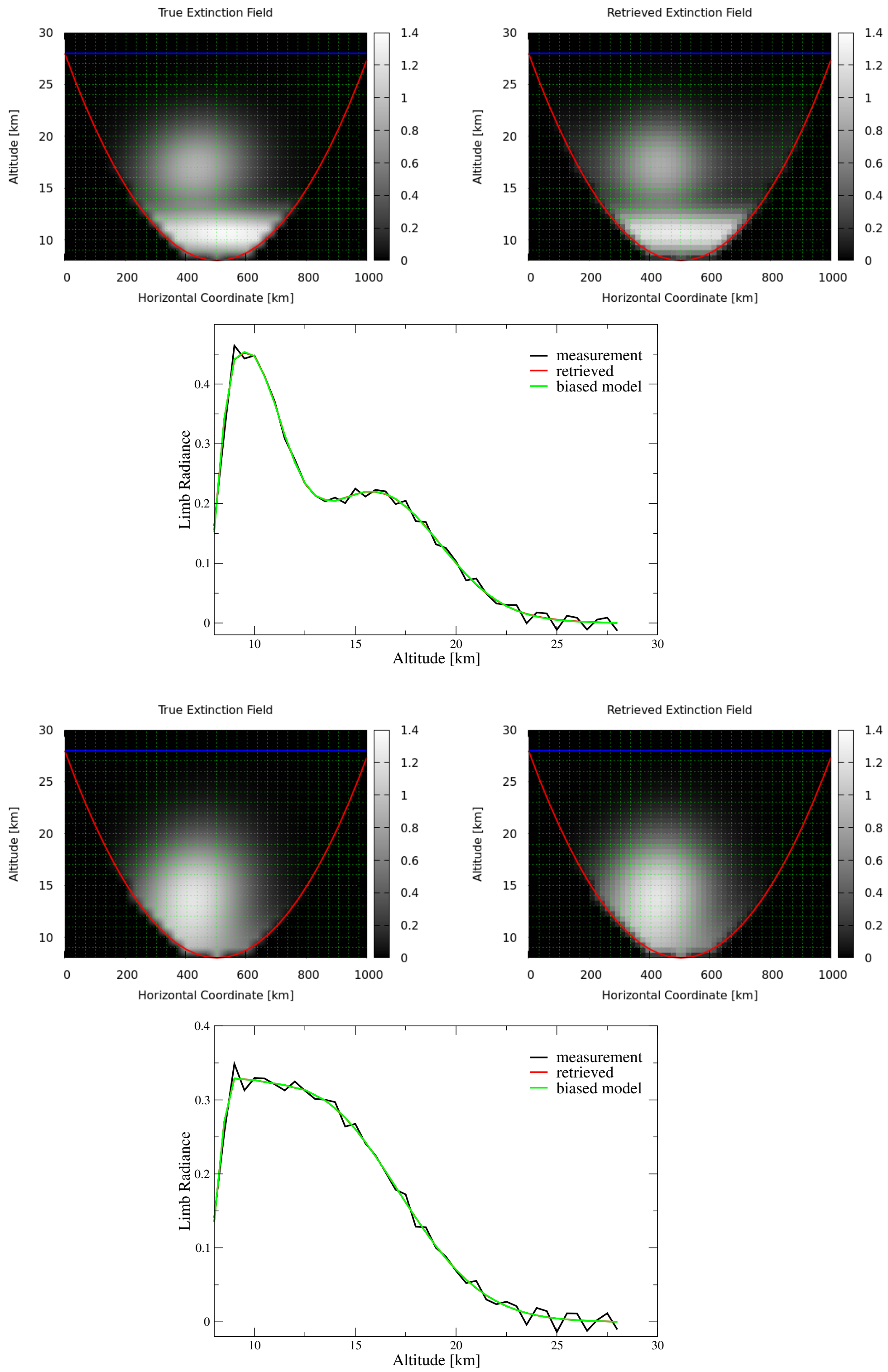

Figure 10. Aerosol extinction retrievals for Scenarios 1 and 2: a vertically broad aerosol distribution with lower and elevated structures, and a smoother compact lower-stratospheric layer. The extinction coefficients are scaled by 10^3 km^{-1}. Red line overlaps green line at the bottom plot.

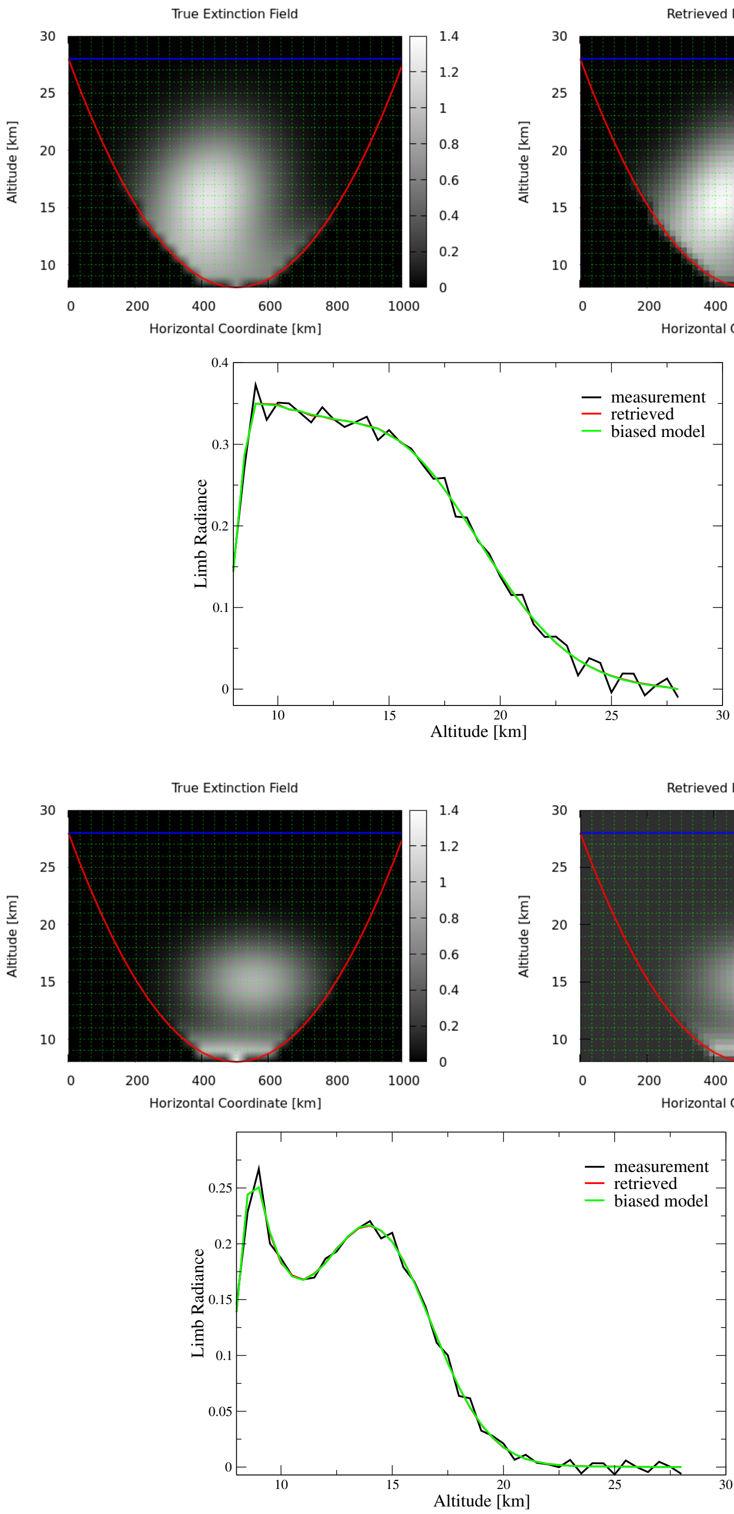

Figure 11. Aerosol extinction retrievals for Scenarios 3 and 4: a broad vertically elongated distribution and a compact isolated elevated plume. The extinction coefficients are scaled by $10^3\,\mathrm{km}^{-1}$.

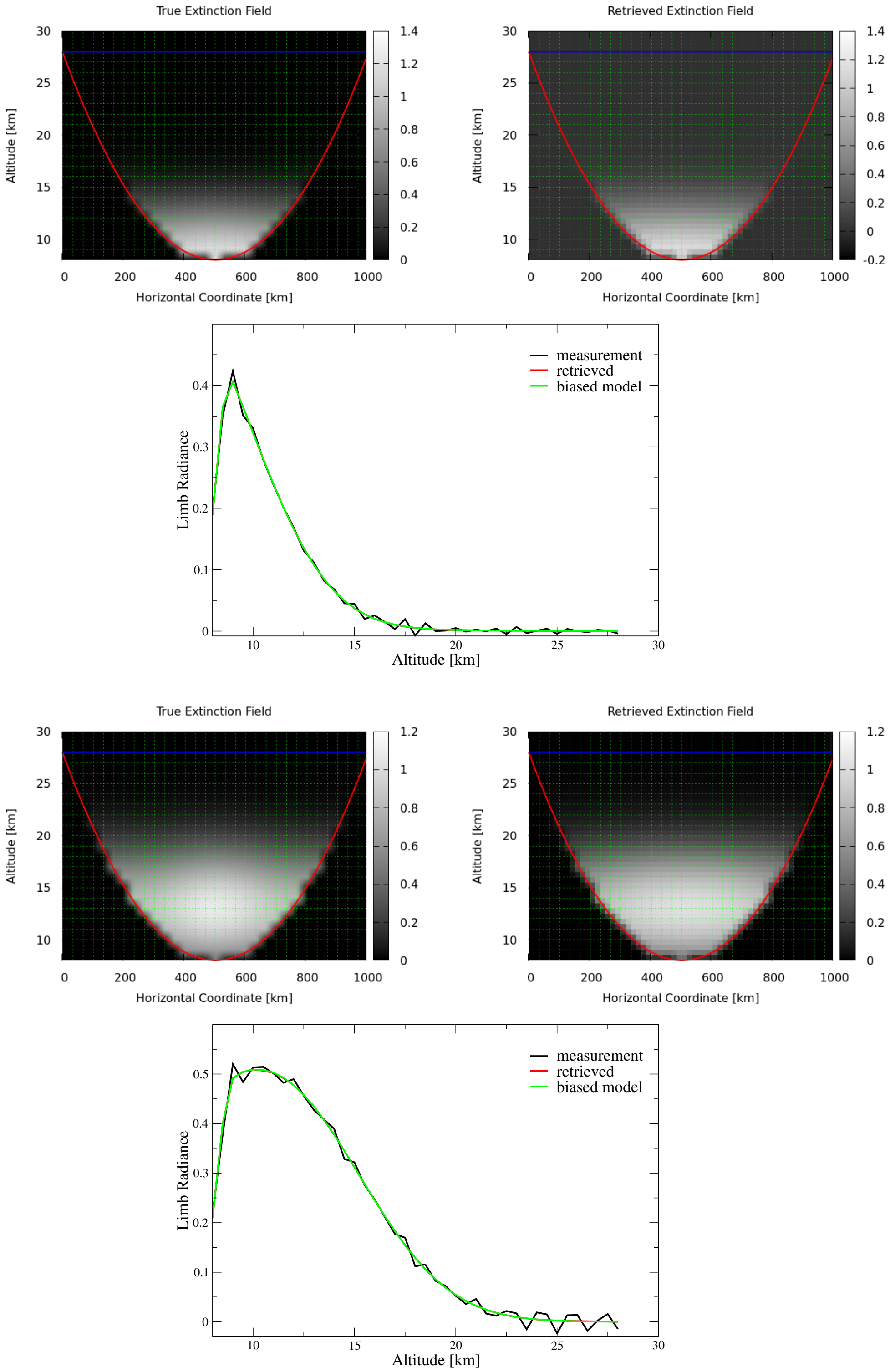

Figure 12. Aerosol extinction retrievals for Scenarios 5 and 6: a shallow low-altitude layer and a broad aerosol layer occupying a large part of the retrieval domain. The extinction coefficients are scaled by $10^3\ \mathrm{km}^{-1}$. The green line at the bottom of the plot overlaps with the red line.

4. Conclusions

In this work, we have investigated the feasibility of retrieving stratospheric aerosol extinction fields from GEO–LEO limb measurements using a dedicated inversion methodology. Two complementary retrieval strategies have been considered: a radial-grid formulation, in which the radial extinction profile and its horizontal extent are retrieved under the assumption of horizontal homogeneity within the aerosol support region, and a parametric formulation, in which the aerosol extinction field is represented by a small number of physically motivated parameters. The numerical experiments demonstrate that both formulations provide stable and physically meaningful reconstructions when combined with appropriate regularization and prior information.

The numerical results show that the radial-grid retrieval strategy is capable of reproducing the dominant aerosol structures over a broad range of synthetic scenarios. The reconstructed radiances agree closely with the synthetic measurements, while the extinction errors remain moderate, typically between approximately 5% and 12%. Broad and vertically smooth aerosol layers are reconstructed more accurately than narrow or strongly localized structures, reflecting the limited information content of the limb measurements and the smoothing inherent in regularized inversion. Although the inverse problem remains strongly ill-conditioned, the averaging kernels and the effective degrees of freedom indicate that the GEO–LEO measurements contain substantial independent information on the vertical aerosol distribution.

The parametric retrieval strategy further improves the conditioning of the inverse problem. Owing to the reduced number of unknowns and the incorporation of prior structural information, the condition numbers of the regularized Hessian are reduced by approximately one to two orders of magnitude while maintaining a high information content. The retrieved extinction fields are smooth, physically plausible, and provide excellent fits to the synthetic measurements. However, these favourable results should be interpreted with some caution because the synthetic extinction fields were generated using the same parametric representation employed in the inversion. Larger reconstruction errors can therefore be expected when the true aerosol distribution cannot be represented adequately by the adopted parameterization.

The numerical experiments also demonstrate the importance of incorporating external information into the retrieval. The use of aerosol optical thickness observations to constrain the horizontal extent of the aerosol field significantly stabilizes the radial-grid inversion, while the parametric formulation illustrates how physically motivated parameterizations can further reduce the ill-posedness of the inverse problem. The results indicate that the radial-grid and parametric formulations are complementary rather than competing approaches. The radial-grid formulation is more appropriate when little prior information is available and arbitrary aerosol structures must be represented, whereas the parametric formulation is preferable when the dominant aerosol morphology can be described by a limited number of physically meaningful components.

The present study has several limitations. The retrieval methodology has been evaluated using synthetic measurements generated from the same forward model employed in the inversion, augmented by additive Gaussian noise and conservative systematic forward-model errors. The forward model is based on the single-scattering approximation, which is appropriate for the optically thin stratospheric aerosol layers considered here but would not be sufficient for optically thick aerosol. Furthermore, the numerical experiments neglect several instrument- and mission-specific effects, including pointing and timing errors, detector calibration uncertainties, background solar radiation, and orbital navigation errors. Consequently, the reported reconstruction accuracies should be regarded as demonstrating the feasibility of the proposed inversion methodology rather than the expected performance of a complete operational retrieval system.

Overall, the GEO–LEO observation geometry appears to provide favourable conditions for localized atmospheric limb sounding by combining high vertical sensitivity with a slowly varying observation geometry. Within the retrieval scenarios considered in this work, the proposed inversion methodology provides stable reconstructions with encouraging accuracy despite the severe ill-posedness of the underlying inverse problem. These results suggest that GEO–LEO limb observations represent a promising concept for future stratospheric aerosol sounding missions.

Future work will focus on several extensions of the present methodology. These include the assimilation of realistic aerosol optical thickness products [31], the incorporation of more accurate radiative-transfer models accounting for multiple scattering [32], the development of more flexible aerosol parameterizations, and the application of the inversion framework to time-dependent aerosol fields. Another important direction will be the investigation of alternative occultation geometries, such as circular–circular LEO–LEO configurations, which offer substantially broader geographical coverage than GEO–LEO systems. Together, these developments should provide a more comprehensive assessment of the capabilities and limitations of future satellite-based aerosol limb-sounding missions.

Author Contributions: Conceptualization, A.D. (Alexandru Doicu), D.S.E., D.G., and A.D. (Adrian Doicu); methodology, A.D. (Alexandru Doicu) and D.S.E.; formal analysis, D.G. and A.D. (Adrian Doicu); writing—original draft preparation, A.D. (Alexandru Doicu), D.S.E., D.G., and A.D. (Adrian Doicu); writing—review and editing, A.D. (Alexandru Doicu), D.S.E., D.G., and A.D. (Adrian Doicu). All authors have read and agreed to the published version of the manuscript.

Funding: This research received no external funding.

Institutional Review Board Statement: Not applicable.

Informed Consent Statement: Not applicable.

Data Availability Statement: No observational datasets were used in this study. The results are based on synthetic numerical simulations generated within the described computational framework. Data are contained within the article. Telemetry-data of TDP1 or Sentinel-1A are not proprietary to the authors and therefore cannot be shared.

Acknowledgments: Authors thank F. Lippert for providing the map of OISL-grazing, and Tesat-Spacecom GmbH for providing telemetry data of grazing tests between Alphasat-TDP1 and Sentinel-1A.

Conflicts of Interest: The authors declare no conflicts of interest.

Appendix A. GEO–LEO Limb Geometry

The purpose of this appendix is to derive the equations governing the tangent-point geometry, the geographic evolution of the tangent-point projection, and the temporal evolution of the observation plane. The formulation is intended primarily for retrieval studies and therefore emphasizes the dominant geometric effects while neglecting higher-order orbital perturbations. The observation geometry for a GEO–LEO limb retrieval configuration is illustrated in Figure 2.

LEO satellite position. The LEO satellite is assumed to move on a circular orbit with orbital radius $R_{\mathrm{L}} = R_{\mathrm{Earth}} + h_{\mathrm{L}}$, where R_{Earth} denotes the Earth radius and h_{L} is the orbital altitude. The following simplifying assumptions are adopted:

1. The orbit is circular.
2. Orbital perturbations caused by Earth oblateness, atmospheric drag, luni-solar perturbations, and solar radiation pressure are neglected.
3. The orbital plane is assumed to remain fixed during the considered time interval.
4. The orbital elements are treated as constant during the simulation period.

These assumptions define an idealized orbital model intended to isolate the dominant geometric effects governing the limb observation geometry. The same model is employed both for short-term simulations of individual limb scans and for long-term simulations of temporal evolution and global geographic coverage.

The orbital plane is characterized by the inclination angle I, defined as the angle between the orbital plane and the equatorial plane, and by the right ascension of the ascending node (RAAN), denoted by Ω. The RAAN specifies the orientation of the line of nodes, i.e., the intersection between the orbital plane and the equatorial plane, measured from the positive X-axis in the equatorial plane. The orbital angular coordinate $u(t)$ denotes the argument of latitude, i.e., the angular position of the satellite measured within the orbital plane from the ascending node. Under the circular-orbit approximation,

$$u(t) = u_0 \pm \omega_{\mathrm{L}} t, \tag{A1}$$

where

$$\omega_{\mathrm{L}} = \sqrt{\frac{\mu}{R_{\mathrm{L}}^3}}, \tag{A2}$$

is the orbital angular velocity and $\mu = 398{,}600.44 \quad \mathrm{km}^3\,\mathrm{s}^{-2}$ is the Earth gravitational parameter. The sign in Equation (A1) is selected such that the tangent altitude decreases during the simulated measurement interval, corresponding to a descending limb scan. The position vector of the LEO satellite in the inertial frame is written as

$$\mathbf{R}_{\mathrm{L}}(t) = x_{\mathrm{L}}(t)\widehat{\mathbf{X}} + y_{\mathrm{L}}(t)\widehat{\mathbf{Y}} + z_{\mathrm{L}}(t)\widehat{\mathbf{Z}}, \tag{A3}$$

where

$$x_{\mathrm{L}}(t) = R_{\mathrm{L}}[\cos\Omega\cos u(t) - \sin\Omega\sin u(t)\cos I], \tag{A4}$$

$$y_{\mathrm{L}}(t) = R_{\mathrm{L}}[\sin\Omega\cos u(t) + \cos\Omega\sin u(t)\cos I], \tag{A5}$$

$$z_{\mathrm{L}}(t) = R_{\mathrm{L}}\sin u(t)\sin I. \tag{A6}$$

The explicit inclusion of the RAAN allows the LEO orbital plane to rotate longitudinally with respect to the GEO meridian plane. Consequently, the geographic distribution of the tangent points depends not only on the inclination I, but also on the relative orientation between the GEO satellite longitude and the LEO orbital plane. In realistic GEO–LEO configurations involving near-polar Sun-synchronous satellites, grazing limb observations may therefore occur preferentially at high latitudes, whereas equatorial grazing events may be comparatively less frequent.

GEO satellite position. The GEO satellite is assumed to move on a circular equatorial orbit of radius R_{G}. Since a geostationary satellite remains fixed relative to the Earth surface, its inertial angular position changes with the Earth angular velocity ω_{E}. Assuming, without loss of generality, that the GEO satellite lies on the positive X-axis at $t = 0$, its angular position in the inertial frame is

$$\phi(t) = \omega_{\mathrm{E}} t, \tag{A7}$$

The GEO satellite position vector is therefore

$$\mathbf{R}_{\mathrm{G}}(t) = R_{\mathrm{G}}\cos\phi(t)\widehat{\mathbf{X}} + R_{\mathrm{G}}\sin\phi(t)\widehat{\mathbf{Y}}, \tag{A8}$$

Tangent altitude. For each measurement time t_m, the line segment connecting GEO and LEO is written as

$$\mathbf{l}(s;t_m) = \mathbf{R}_{\mathrm{G}}(t_m) + s\mathbf{d}(t_m), \qquad 0 \le s \le 1, \tag{A9}$$

where $\mathbf{d}(t) = \mathbf{R}_\mathrm{L}(t) - \mathbf{R}_\mathrm{G}(t)$. The tangent point is defined as the point on the line of sight closest to the Earth center. Minimization of the squared distance $\|\mathbf{R}_\mathrm{G} + s\mathbf{d}\|^2$with respect to s yields

$$s_\mathrm{T} = -\frac{\mathbf{R}_\mathrm{G} \cdot \mathbf{d}}{\mathbf{d} \cdot \mathbf{d}}. \tag{A10}$$

The corresponding tangent-point vector in the reference frame $OXYZ$ is

$$\mathbf{t}(t_m) = \mathbf{R}_\mathrm{G}(t_m) + s_\mathrm{T}(t_m)\mathbf{d}(t_m). \tag{A11}$$

The tangent radius and tangent altitude are then $R_\mathrm{T}(t_m) = \|\mathbf{t}(t_m)\|$ and $h_\mathrm{T}(t_m) = R_\mathrm{T}(t_m) - R_\mathrm{Earth}$, respectively. For a physically admissible limb ray, the closest point should lie on the finite GEO–LEO segment, i.e., $0 \leq s_\mathrm{T} \leq 1$. If this condition is violated, the closest point belongs to the infinite extension of the line but not to the actual GEO–LEO segment. In that case, the computed tangent point is not physically meaningful for the finite observation path. In addition, if $h_\mathrm{T}(t_m) < 0$, the line of sight intersects the Earth and the corresponding ray is not an admissible limb measurement.

Geographic evolution of the tangent-point projection. The unit vector in the direction of the tangent point is $\widehat{\mathbf{n}}_\mathrm{T}(t_m) = \mathbf{t}(t_m)/R_\mathrm{T}(t_m)$, and the corresponding point on the Earth surface can be written as

$$\mathbf{R}_\mathrm{ET}(t_m) = R_\mathrm{Earth}\widehat{\mathbf{n}}_\mathrm{T}(t_m) = R_\mathrm{Earth}[\widehat{n}_\mathrm{Tx}(t_m)\widehat{\mathbf{X}} + \widehat{n}_\mathrm{Ty}(t_m)\widehat{\mathbf{Y}} + \widehat{n}_\mathrm{Tz}(t_m)\widehat{\mathbf{Z}}]. \tag{A12}$$

To determine the geographic latitude and longitude of the tangent-point projection, an Earth-fixed reference frame $Ox_\mathrm{E}y_\mathrm{E}z_\mathrm{E}$ is introduced. This frame is obtained from the inertial frame by a rotation around the Z-axis by the Earth rotation angle $\phi_\mathrm{E}(t) = \omega_\mathrm{E}t$. In the Earth-fixed coordinate system, the position vector $\mathbf{R}_\mathrm{ET}(t_m)$ is then

$$\mathbf{R}_\mathrm{ET}(t_m) = x_\mathrm{ET}(t_m)\widehat{\mathbf{x}}_\mathrm{E} + y_\mathrm{ET}(t_m)\widehat{\mathbf{y}}_\mathrm{E} + z_\mathrm{ET}(t_m)\widehat{\mathbf{z}}_\mathrm{E}, \tag{A13}$$

where

$$x_\mathrm{ET}(t_m) = R_\mathrm{Earth}[\widehat{n}_\mathrm{Tx}(t_m)\cos\phi_\mathrm{E}(t_m) + \widehat{n}_\mathrm{Ty}(t_m)\sin\phi_\mathrm{E}(t_m)], \tag{A14}$$

$$y_\mathrm{ET}(t_m) = R_\mathrm{Earth}[-\widehat{n}_\mathrm{Tx}(t_m)\sin\phi_\mathrm{E}(t_m) + \widehat{n}_\mathrm{Ty}(t_m)\cos\phi_\mathrm{E}(t_m)], \tag{A15}$$

$$z_\mathrm{ET}(t_m) = R_\mathrm{Earth}\widehat{n}_\mathrm{Tz}(t_m). \tag{A16}$$

The latitude and longitude $(\varphi_\mathrm{ET}, \lambda_\mathrm{ET})$ of the position vector $\mathbf{R}_\mathrm{ET}(t_m)$ in the Earth-fixed coordinate system are computed as

$$\varphi_\mathrm{ET}(t_m) = \arcsin\left(\frac{z_\mathrm{ET}(t_m)}{R_\mathrm{Earth}}\right), \tag{A17}$$

$$\lambda_\mathrm{ET}(t_m) = \arctan 2(y_\mathrm{ET}(t_m), x_\mathrm{ET}(t_m)). \tag{A18}$$

Temporal evolution of the observation plane. The instantaneous GEO–LEO observation plane at time t_m is the plane spanned by the vectors $\mathbf{R}_\mathrm{G}(t_m)$ and $\mathbf{R}_\mathrm{L}(t_m)$, since both vectors originate at the Earth center. Therefore, a normal vector to this plane is given by the cross product $\mathbf{n}(t_m) = \mathbf{R}_\mathrm{G}(t_m) \times \mathbf{R}_\mathrm{L}(t_m)$, and the unit normal vector is

$$\widehat{\mathbf{n}}(t_m) = \frac{\mathbf{R}_\mathrm{G}(t_m) \times \mathbf{R}_\mathrm{L}(t_m)}{\|\mathbf{R}_\mathrm{G}(t_m) \times \mathbf{R}_\mathrm{L}(t_m)\|}. \tag{A19}$$

If $\|\mathbf{R}_\mathrm{G}(t_m) \times \mathbf{R}_\mathrm{L}(t_m)\| = 0$, then the GEO vector and the LEO vector are collinear, and the observation plane is degenerate. To quantify the temporal evolution of the observation plane, a reference plane is chosen at the initial time $t_1 = 0$, with unit normal vector $\widehat{\mathbf{n}}_0 = \widehat{\mathbf{n}}(t_1)$. For each later time t_m, the angle between the reference plane and the instantaneous plane is computed from the dot product of the unit normals: $\cos\psi_m = \left|\widehat{\mathbf{n}}_0 \cdot \widehat{\mathbf{n}}(t_m)\right|$. Thus,

$$\psi_m = \arccos\min(1, \left|\widehat{\mathbf{n}}_0 \cdot \widehat{\mathbf{n}}(t_m)\right|). \tag{A20}$$

The absolute value is used because the two normals $\widehat{\mathbf{n}}$ and $-\widehat{\mathbf{n}}$ define the same plane. Therefore, the angle between two planes is independent of the orientation of their normal vectors.

Temporal regimes. Two different temporal regimes are considered in the present study.

1. For short time scales relevant to individual limb scans, typically lower than 20 s, the Earth rotation can be neglected. In this case, $\phi_{\mathrm{E}}(t) \approx 0$, and the Earth-fixed and inertial frames practically coincide. Consequently, the temporal evolution of the tangent altitude and the observation geometry is governed almost entirely by the LEO orbital motion. From Equation (A19) and $\mathbf{R}_{\mathrm{G}}(t_m) \approx R_{\mathrm{G}}\widehat{\mathbf{X}}$, it follows that during the occultation interval, the GEO–LEO observation plane rotates about the direction of the vector $\mathbf{R}_{\mathrm{G}}$.
2. For long time scales, relevant to the analysis of temporal evolution and geographic coverage over several orbital revolutions or multiple days, the Earth rotation must be included explicitly. In this regime, the Earth rotation causes a continuous drift of the tangent-point geographic coordinates relative to the Earth surface, thereby producing the geographic coverage patterns shown in the numerical simulations.

Appendix B. Small-Angle Multiple-Scattering Model

In this appendix, we describe the small-angle approximation to the radiative transfer equation for an inhomogeneous slab. The method assumes paraxial propagation and strongly forward-peaked scattering, such that all relevant propagation and scattering angles remain small [33]. The atmosphere is represented by homogeneous layers with transversely uniform optical properties. Furthermore, the incident beam and the forward-scattering phase-function peak are approximated by Gaussian functions, while polarization, refraction, large-angle scattering, and backscattering are neglected. The formulation extends the methodology presented in Ref. [24] to the case of an inhomogeneous slab.

For each limb path, a local Cartesian coordinate system $Oxyz$ is introduced. The z-axis is aligned with the propagation direction of the incident beam. Therefore, the coordinate z coincides with the path coordinate. The coordinates x and y describe the transverse position relative to the beam axis. The transverse position vector is $\boldsymbol{\rho} = (x, y)$ with magnitude $\rho = \sqrt{x^2 + y^2}$. The propagation direction of the incident beam is $\widehat{\boldsymbol{\Omega}} = (\Omega_{\mathrm{x}}, \Omega_{\mathrm{y}}, \Omega_{\mathrm{z}})$. Under the small-angle approximation, $|\Omega_{\mathrm{x}}| \ll 1$, $|\Omega_{\mathrm{y}}| \ll 1$, and $\Omega_{\mathrm{z}} \approx 1$. The transverse angular vector is $\boldsymbol{\Omega}_{\perp} = (\Omega_{\mathrm{x}}, \Omega_{\mathrm{y}})$ with magnitude $\Omega_{\perp} = \sqrt{\Omega_{\mathrm{x}}^2 + \Omega_{\mathrm{y}}^2}$.

The atmosphere is divided into N homogeneous layers. The layer boundaries are $z_0 = 0, z_1, \ldots, z_N = H$, and the thickness of layer k is $\Delta z_k = z_k - z_{k-1}$. Within layer k, the optical properties are assumed constant:

$$\sigma(z) = \sigma_k,\ \ \omega_0(z) = \omega_{0,k},\ \ P(\psi, z) = P_k(\psi), \tag{A21}$$

where σ_k is the extinction coefficient, $\omega_{0,k}$ is the single-scattering albedo, $P_k(\psi)$ is the scattering phase function, and ψ is the scattering angle.

The small-angle radiative transfer equation for the (total) radiance $I(z, \boldsymbol{\rho}, \boldsymbol{\Omega}_{\perp})$ is

$$\left(\frac{\partial}{\partial z} + \boldsymbol{\Omega}_{\perp} \cdot \nabla_{\boldsymbol{\rho}} + \sigma_k\right) I = \omega_{0,k}\sigma_k \int P_k(\boldsymbol{\Omega}_{\perp} - \boldsymbol{\Omega}'_{\perp}) I(z, \boldsymbol{\rho}, \boldsymbol{\Omega}'_{\perp})\, \mathrm{d}\boldsymbol{\Omega}'_{\perp}, \tag{A22}$$

where the term $\boldsymbol{\Omega}_\perp \cdot \nabla_\rho$ describes free propagation, whereas the integral term describes multiple forward scattering.

The Fourier transform of the radiance is defined by

$$\widehat{I}(z, \boldsymbol{\eta}, \boldsymbol{\xi}) = \frac{1}{(2\pi)^2} \int I(z, \boldsymbol{\rho}, \boldsymbol{\Omega}_\perp) e^{\mathrm{j}(\boldsymbol{\eta}\cdot\boldsymbol{\rho}+\boldsymbol{\xi}\cdot\boldsymbol{\Omega}_\perp)} \,\mathrm{d}\boldsymbol{\rho}\,\mathrm{d}\boldsymbol{\Omega}_\perp, \tag{A23}$$

where the vectors $\boldsymbol{\eta} = (\eta_x, \eta_y)$ and $\boldsymbol{\xi} = (\xi_x, \xi_y)$ are the Fourier variables associated with $\boldsymbol{\rho}$ and $\boldsymbol{\Omega}_\perp$, respectively.

At the top of the atmosphere, the beam is assumed to be Gaussian in both position and direction:

$$I_0(\boldsymbol{\rho}, \boldsymbol{\Omega}_\perp) = F_0 \frac{\beta^2\gamma^2}{\pi^2} \exp(-\beta^2\Omega_\perp^2 - \gamma^2\rho^2). \tag{A24}$$

The parameter F_0 is the total beam power. The parameter β controls the angular divergence, with larger values of β corresponding to a more highly collimated beam. The parameter γ controls the beam width, with larger values of γ corresponding to a narrow beam. Specifically, the factor $\exp(-\gamma^2\rho^2)$ describes the transverse spatial profile of the beam, whereas the factor $\exp(-\beta^2\Omega_\perp^2)$ describes its angular distribution. Consequently, Equation (A24) accounts for both the finite beam width and the angular divergence of the beam The Fourier transform of the incident beam is

$$\widehat{I}_0(\boldsymbol{\eta}, \boldsymbol{\xi}) = \frac{F_0}{(2\pi)^2} \exp\Big(-\frac{\eta^2}{4\gamma^2} - \frac{\xi^2}{4\beta^2}\Big), \tag{A25}$$

where $\eta = |\boldsymbol{\eta}|$ and $\xi = |\boldsymbol{\xi}|$.

In layer k, the scattering phase function is assumed to have a Gaussian form

$$P_k(\boldsymbol{\psi}) = \frac{\alpha_k^2}{2\pi} \exp\Big(-\frac{\alpha_k^2|\boldsymbol{\psi}|^2}{2}\Big), \tag{A26}$$

where $\boldsymbol{\psi} = \boldsymbol{\Omega}_\perp - \boldsymbol{\Omega}'_\perp$ is the angular difference vector. The parameter α_k controls the width of the forward-scattering peak, with larger values of α_k corresponding to a narrower forward peak and smaller scattering angles. For each layer k, the parameter α_k is determined from the actual aerosol phase function, obtained from particle-scattering calculations or measurements. It is chosen so that the Gaussian phase function reproduces the angular width of the forward-scattering peak, for example by matching its mean-square scattering angle or by fitting the Gaussian model directly to the forward lobe. The Fourier transform of the phase function is

$$\widehat{P}_k(\boldsymbol{\xi}) = \frac{1}{2\pi} \int P_k(\boldsymbol{\psi}) \,\exp(\mathrm{j}\boldsymbol{\xi}\cdot\boldsymbol{\psi})\mathrm{d}\boldsymbol{\psi}. \tag{A27}$$

Because the Gaussian phase function depends only on the magnitude of $\boldsymbol{\psi}$ its Fourier transform is rotationally symmetric and depends only on $\xi = |\boldsymbol{\xi}|$. Consequently, the two-dimensional Fourier transform reduces to a Hankel transform,

$$\widehat{P}_k(\xi) = \int_0^\infty J_0(\xi\psi) P_k(\psi)\psi \,\mathrm{d}\psi, \tag{A28}$$

where J_0 is the Bessel function of order zero. Substituting the Gaussian phase function into the above integral yields

$$\widehat{P}_k(\xi) = \frac{1}{2\pi} \exp\Big(-\frac{\xi^2}{2\alpha_k^2}\Big). \tag{A29}$$

Equivalently, using vector notation,

$$\widehat{P}_k(\boldsymbol{\xi}) = \frac{1}{2\pi} \exp\left(-\frac{|\boldsymbol{\xi}|^2}{2\alpha_k^2}\right). \quad \text{(A30)}$$

Inside layer k, the Fourier-transformed radiance is

$$\widehat{I}_k(z, \boldsymbol{\eta}, \boldsymbol{\xi}) = \widehat{I}_k^{\text{in}}(\boldsymbol{\eta}, \boldsymbol{\xi} + z\boldsymbol{\eta}) \exp[-\sigma_k z + \Omega_k(z, \boldsymbol{\eta}, \boldsymbol{\xi})], \quad \text{(A31)}$$

for $0 \le z \le \Delta z_k$, where $\widehat{I}_k^{\text{in}}(\boldsymbol{\eta}, \boldsymbol{\xi})$ denotes the Fourier-transformed radiance entering layer k, and $\Omega_k(z, \boldsymbol{\eta}, \boldsymbol{\xi})$ is the scattering exponent given by

$$\Omega_k(z, \boldsymbol{\eta}, \boldsymbol{\xi}) = 2\pi\omega_{0,k}\sigma_k \int_0^z \widehat{P}_k(\boldsymbol{\xi} + z'\boldsymbol{\eta})\, \mathrm{d}z'. \quad \text{(A32)}$$

The radiance is continuous across the interface between two adjacent layers. Thus, $I_{k+1}^{\text{in}} = I_k^{\text{out}}$, meaning that the outgoing radiance of one layer becomes the incoming radiance of the next layer. Consequently, in the Fourier space, we have $\widehat{I}_{k+1}^{\text{in}} = \widehat{I}_k^{\text{out}}$. The outgoing radiance from layer k is

$$\widehat{I}_k^{\text{out}}(\boldsymbol{\eta}, \boldsymbol{\xi}) = \widehat{I}_k(\Delta z_k, \boldsymbol{\eta}, \boldsymbol{\xi}), \quad \text{(A33)}$$

yielding

$$\widehat{I}_{k+1}^{\text{in}}(\boldsymbol{\eta}, \boldsymbol{\xi}) = \widehat{I}_k^{\text{in}}(\boldsymbol{\eta}, \boldsymbol{\xi} + \Delta z_k \boldsymbol{\eta}) \exp[-\sigma_k \Delta z_k + \Omega_k(\Delta z_k, \boldsymbol{\eta}, \boldsymbol{\xi})]. \quad \text{(A34)}$$

The incoming radiance in the first layer is $\widehat{I}_1^{\text{in}} = \widehat{I}_0$. For $k = 1, 2, \ldots, N$, the outgoing radiance is computed recursively as

$$\widehat{I}_k^{\text{out}} = \widehat{I}_k^{\text{in}}(\boldsymbol{\eta}, \boldsymbol{\xi} + \Delta z_k \boldsymbol{\eta}) \exp[-\sigma_k \Delta z_k + \Omega_k(\Delta z_k, \boldsymbol{\eta}, \boldsymbol{\xi})]. \quad \text{(A35)}$$

After propagation through all layers, $\widehat{I}_{\text{exit}} = \widehat{I}_N^{\text{out}}$, and the radiance at the exit plane is obtained by the inverse Fourier transform

$$I_{\text{exit}}(\boldsymbol{\rho}, \boldsymbol{\Omega}_\perp) = (2\pi)^{-2} \int \widehat{I}_{\text{exit}}(\boldsymbol{\eta}, \boldsymbol{\xi}) e^{-\mathrm{j}(\boldsymbol{\eta}\cdot\boldsymbol{\rho} + \boldsymbol{\xi}\cdot\boldsymbol{\Omega}_\perp)}\, \mathrm{d}\boldsymbol{\eta}\, \mathrm{d}\boldsymbol{\xi}. \quad \text{(A36)}$$

The function $I_{\text{exit}}(\boldsymbol{\rho}, \boldsymbol{\Omega}_\perp)$ represents the complete spatial-angular radiance distribution emerging from the multilayer atmosphere.

The irradiance at the exit plane is obtained by integrating the radiance over all propagation directions,

$$N_{\text{exit}}(\boldsymbol{\rho}) = \int I_{\text{exit}}(\boldsymbol{\rho}, \boldsymbol{\Omega}_\perp)\, \mathrm{d}\boldsymbol{\Omega}_\perp. \quad \text{(A37)}$$

Using the inverse Fourier representation, this becomes

$$N_{\text{exit}}(\boldsymbol{\rho}) = \int \widehat{I}_{\text{exit}}(\boldsymbol{\eta}, 0) \exp(-\mathrm{j}\boldsymbol{\eta} \cdot \boldsymbol{\rho})\, \mathrm{d}\boldsymbol{\eta}. \quad \text{(A38)}$$

Thus, only the Fourier component $\boldsymbol{\xi} = 0$ is needed to compute the irradiance. If the emerging beam is cylindrically symmetric with respect to the local beam axis, the irradiance depends only on $\rho = |\boldsymbol{\rho}|$. In this case,

$$N_{\text{exit}}(\rho) = 2\pi \int_0^\infty J_0(\eta\rho) \widehat{I}_{\text{exit}}(\eta, 0) \eta\, \mathrm{d}\eta. \quad \text{(A39)}$$

Finally, we consider a circular detector of radius R located in the exit plane and centered on the local beam axis. The power received by the detector is obtained by integrating the irradiance over the detector area,

$$P_{\text{det}} = 2\pi \int_0^R N_{\text{exit}}(\rho)\rho \, d\rho. \tag{A40}$$

Substituting the cylindrical representation of the irradiance gives

$$P_{\text{det}} = 4\pi^2 R \int_0^\infty J_1(\eta R) \widehat{I}_{\text{exit}}(\eta, 0) \, d\eta, \tag{A41}$$

where J_1 is the Bessel function of order one.

In summary, the algorithm consists of computing the exiting radiance in Fourier space, $\widehat{I}_{\text{exit}}(\boldsymbol{\eta}, \boldsymbol{\xi})$ by means of the recurrence relation (A35), followed by the computation of the power received by the detector, P_{det} using Equation (A41).

Appendix C. Details of the Multistart Optimization Algorithm

Section 2.4 presents the main steps of the multistart optimization algorithm used in the retrieval procedure. The present appendix provides additional implementation details, including candidate-point generation, selection and validation strategies, local optimization methods, discrepancy-principle filtering, regularization-parameter selection, and the computation of information-content measures. These details are included for completeness and reproducibility.

1. Candidate starting points can be generated by pseudo-random number generators [34,35], chaotic methods [36–38], low discrepancy methods (Halton, Sobol, and Faure sequences), Latin hypercube sampling [39], quasi-oppositional differential evolution [40,41], and centroidal Voronoi tessellation [42].
2. The selection of a reduced starting set can be performed in different ways.
   (a) The distance-filter strategy scans the ranked list and accepts a candidate only if it is sufficiently far from all previously selected points, thereby retaining good starting points while avoiding clustering.
   (b) The importance-sampling strategy randomly selects candidates with probabilities favoring smaller residual-function values and applies the same distance criterion to preserve diversity.
   (c) The hybrid strategy first applies deterministic distance filtering to the ranked list and, if necessary, fills the remaining positions by importance sampling.
   (d) As an alternative to this purely sampling-based preselection, the evolutionary approach [43] can be used to improve the generation of starting points. In this case, a population of parameter vectors is evolved by a JADE-type differential evolution algorithm with mutation, crossover, archive-based diversity, and adaptive control parameters [44]. After a fixed number of generations, the population is sorted according to the residual, and the best N_{start0} parameter vectors are retained as starting points.
3. The multistart algorithm screens candidate starts $\mathbf{x}_{0k}$ using the following standard tests:
   (a) Function-distance test versus prior starts: Reject any point whose objective value is no better than a previously successful start and lies within the typical distance of that start. Specifically, if there exists a previously used starting point $\mathbf{x}_{0l}$ (that led to a successful solution) such that

$$\mathcal{F}(\mathbf{x}_{0k}) < \mathcal{F}(\mathbf{x}_{0l}) \text{ and } \|\mathbf{x}_{0k} - \mathbf{x}_{0l}\| < R_{\text{T}}, \tag{A42}$$

   where R_{T} denotes the typical distance, then $\mathbf{x}_{0k}$ is not considered a valid starting point.

(b) Basin exclusion: Reject any point that lies within the basin of attraction of a known solution. Specifically, if there exists a previously found solution $\mathbf{x}_{\mathrm{S}n}$ such that

$$\|\mathbf{x}_{0k} - \mathbf{x}_{\mathrm{S}n}\| < R_{\mathrm{SB}}(n), \tag{A43}$$

where $R_{\mathrm{SB}}(n)$ denotes the radius of the basin of attraction of the solution $\mathbf{x}_{\mathrm{S}n}$, then $\mathbf{x}_{0k}$ is considered to belong to that basin and is therefore rejected. For the solution $\mathbf{x}_{\mathrm{S}n}$, the radius of the basin of attraction is estimated as $R_{\mathrm{SB}}(n) = \max_{i \geq N_{\mathrm{B}}} \|\mathbf{x}_{\mathrm{S}n}^{(i)} - \mathbf{x}_{\mathrm{S}n}\|$ under the assumption that once the local search reaches iteration $i \geq N_{\mathrm{B}}$, all subsequent iterates $\mathbf{x}_{\mathrm{S}n}^{(i)}$ remain within the same basin of attraction.

(c) Gradient–distance test versus solutions [45]: Reject any point whose gradient suggests it would converge to an existing solution and which lies closer than the minimum observed spacing between known solutions. Specifically, let

$$d_{\mathrm{Smin}} = \min_{n_1, n_2, n_1 \neq n_2} \|\mathbf{x}_{\mathrm{S}n_1} - \mathbf{x}_{\mathrm{S}n_2}\| \text{ with } \mathbf{x}_{\mathrm{S}n_1}, \mathbf{x}_{\mathrm{S}n_2} \in X_{\mathrm{S}} \tag{A44}$$

be the minimum (pairwise) distance among known solutions, where X_{S} is the set of solutions. If there exists a previously found solution $\mathbf{x}_{\mathrm{S}n}$ for which

$$(\mathbf{x}_{0k} - \mathbf{x}_{\mathrm{S}n})^T [\nabla \mathcal{F}(\mathbf{x}_{0k}) - \nabla \mathcal{F}(\mathbf{x}_{\mathrm{S}n})] > 0 \text{ and } \|\mathbf{x}_{0k} - \mathbf{x}_{\mathrm{S}n}\| < d_{\mathrm{Smin}}, \tag{A45}$$

then the starting point $\mathbf{x}_{0k}$ is rejected.

(d) Gradient–distance test versus prior starts [45]: Reject any point whose gradient indicates it would converge to a previously used starting point and which lies within that point's typical convergence radius. Specifically, if there exists a previously used starting point $\mathbf{x}_{0l}$ (that led to a successful solution) such that

$$(\mathbf{x}_{0k} - \mathbf{x}_{0l})^T [\nabla \mathcal{F}(\mathbf{x}_{0k}) - \nabla \mathcal{F}(\mathbf{x}_{0l})] > 0 \text{ and } \|\mathbf{x}_{0k} - \mathbf{x}_{0l}\| < R_{\mathrm{T}}, \tag{A46}$$

then $\mathbf{x}_{0k}$ is not a valid starting point.

4. In the algorithm implementation, two local solvers are available. The first is the routine DRN2GB from the PORT library [46,47], a derivative-based algorithm for bounded nonlinear least-squares problems that combines Gauss–Newton steps with quasi-Newton corrections. The second is the limited-memory BFGS method [48], which approximates the inverse Hessian by a small number of correction vectors and is well suited for medium- and large-scale problems. Both solvers are designed to solve optimization problems with simple bound constraints on the variables.
5. The discrepancy-principle solutions $\mathbf{x}_{\mathrm{S}}$ are all solutions satisfying the discrepancy condition [49,50]

$$0.1\,\Delta^2 \leq \mathcal{R}(\mathbf{x}_{\mathrm{S}}) \leq 1.2\,\Delta^2,$$

where $\mathcal{R}(\mathbf{x}) = \|\mathbf{F}(\mathbf{x}) - \mathbf{y}^{\delta}\|^2$ is the squared residual, and Δ denotes the noise level. When the true solution $\mathbf{x}^{\dagger}$ is known, the squared noise level can be estimated by $\Delta^2 = \|\mathbf{F}(\mathbf{x}^{\dagger}) - \mathbf{y}^{\delta}\|^2$. This selection criterion is motivated by the discrepancy principle and is intended to retain solutions whose residuals are consistent with the estimated perturbation level. The introduction of the lower residual bound is motivated by the observation that the residual at the final solution is sometimes significantly smaller than the estimated noise level. This behavior is not contradictory and can be explained by several effects.

(a) The perturbation level Δ^2 is computed relative to the exact solution $\mathbf{x}^\dagger$, but the exact solution is generally not the minimizer of the perturbed inverse problem. Since the measurements contain both systematic modeling errors and random perturbations, another parameter vector may reproduce the perturbed data more accurately than the true solution itself. In this sense, the optimization procedure partially compensates for the forward-model mismatch and the random perturbations by moving away from $\mathbf{x}^\dagger$.

(b) The inverse problem is ill-conditioned and often underdetermined. Consequently, different parameter vectors may produce very similar measurement vectors. Some solutions may therefore fit the noisy measurements exceptionally well, even though they differ from the exact solution.

(c) The clustering step acts as a stabilization mechanism. Solutions associated with isolated overfitting minima are less likely to form large and stable clusters, whereas physically meaningful solutions tend to appear repeatedly from different starting points. Selecting cluster centers therefore suppresses many unstable minima while still allowing residuals smaller than Δ^2.

(d) The discrepancy interval $[0.1\,\Delta^2,\, 1.2\,\Delta^2]$ already admits solutions with residuals substantially below Δ^2. Therefore, the occurrence of final residuals smaller than Δ^2 is fully consistent with the admissibility criterion itself. In practice, the fact that these solutions simultaneously yield small reconstruction errors indicates that the multistart–clustering strategy successfully identifies stable regions of parameter space that explain the perturbed measurements while remaining close to the true aerosol extinction field.

6. The regularization parameter α can be chosen either by trial and error or by using the following procedure. Consider a logarithmic sequence of candidate regularization parameters $\{\alpha_1, \alpha_2, \ldots, \alpha_{N_\alpha}\}$. For each value of $\alpha \in \{\alpha_1, \alpha_2, \ldots, \alpha_{N_\alpha}\}$, let $\mathbf{x}_{\mathrm{C}\alpha}$ denote the corresponding minimum-cluster solution, and let $\mathcal{R}(\mathbf{x}_{\mathrm{C}\alpha})$ be its residual value. The optimal value of the regularization parameter is selected as

$$\alpha_{\mathrm{opt}} = \arg\min_{\alpha} \mathcal{R}(\mathbf{x}_{\mathrm{C}\alpha}).$$

This choice yields the smoothest and most stable solution that remains statistically consistent with the data errors.

7. At the solution $\mathbf{x}_\mathrm{S}$ (representing either the minimum-error solution or the minimum-cluster solution corresponding to the regularization parameter α), the averaging kernel matrix is computed as

$$\mathsf{A} = (\mathsf{K}^\mathrm{T}\mathsf{K} + \alpha_{\mathrm{opt}}\mathsf{L}^\mathrm{T}\mathsf{L})^{-1}\mathsf{K}^\mathrm{T}\mathsf{K},$$

where K is the Jacobian matrix evaluated at $\mathbf{x}_\mathrm{S}$. The degrees of freedom for signal are then calculated as $\mathrm{DoF} = \mathrm{trace}(\mathsf{A})$, and the regularized Hessian is given by $\mathsf{H} = \mathsf{K}^\mathrm{T}\mathsf{K} + \alpha_{\mathrm{opt}}\mathsf{L}^\mathrm{T}\mathsf{L}$.

8. In many practical applications, the effective noise level, including both measurement noise and forward-model errors, is unknown. In such cases, the algorithm is first executed using a broad discrepancy-principle interval. The minimum-error solution $\mathbf{x}_\mathrm{S}$ and its residual value $\mathcal{R}(\mathbf{x}_\mathrm{S})$ are then recorded. An estimate of the effective noise level is subsequently defined by $\Delta^2 = 10\mathcal{R}(\mathbf{x}_\mathrm{S})$. In a second run, the minimum-cluster solution is computed using the discrepancy-principle interval $[0.1\Delta^2, 1.2\Delta^2]$.

References

1. Dörner, S.; Pukīte, J.; Kühl, S.; Penning de Vries, M.; Wagner, T. Retrieval of stratospheric aerosol properties from SCIAMACHY limb observations. In Proceedings of the ESA Living Planet Symposium, Bergen, Norway, 28 June–2 July 2010.
2. Rozanov, A.; Pohl, C.; Arosio, C.; Bourassa, A.; Bramstedt, K.; Malinina, E.; Rieger, L.; Burrows, J.P. Retrieval of stratospheric aerosol extinction coefficients from sun-normalized Ozone Mapper and Profiler Suite Limb Profiler (OMPS-LP) measurements. *Atmos. Meas. Tech.* **2024**, *17*, 6677–6695. [CrossRef]
3. Bourassa, A.E.; Degenstein, D.A.; Llewellyn, E.J. Retrieval of stratospheric aerosol size information from OSIRIS limb scattered sunlight spectra. *Atmos. Chem. Phys.* **2008**, *8*, 6375–6380. [CrossRef]
4. Bourassa, A.E.; Degenstein, D.A.; Llewellyn, E.J. Stratospheric aerosol retrieval with Optical Spectrograph and InfraRed Imaging System limb scatter measurements. *J. Geophys. Res. Atmos.* **2007**, *112*, D10217. [CrossRef]
5. Liu, S.; Zhang, P.; Chen, L.; Xu, N.; Duan, M.; Lyu, D. Extraction of Stratospheric Aerosol Extinction Profiles from Limb-Scattering Signals Measured by the BLS onboard the Tiangong-2 Space Laboratory. *Adv. Atmos. Sci.* **2026**, *43*, 1212–1225. [CrossRef]
6. Rault, D.F.; Loughman, R.P. The OMPS Limb Profiler Environmental Data Record Algorithm Theoretical Basis Document and Expected Performance. *IEEE Trans. Geosci. Remote Sens.* **2013**, *51*, 2505–2527. [CrossRef]
7. Chen, Z.; Bhartia, P.K.; Loughman, R.; Colarco, P.; DeLand, M.; Jaross, G.; Taha, G.; Kramarova, N.; Moy, L.; Xu, P. Evaluation of the OMPS/LP stratospheric aerosol extinction product using SAGE III/ISS observations. *Atmos. Meas. Tech.* **2020**, *13*, 3471–3485. [CrossRef]
8. Rieger, L.A.; Malinina, E.P.; Rozanov, A.V.; Burrows, J.P.; Bourassa, A.E.; Degenstein, D.A. A study of the approaches used to retrieve aerosol extinction, as applied to limb observations made by OSIRIS and SCIAMACHY. *Atmos. Meas. Tech.* **2018**, *11*, 3433–3445. [CrossRef]
9. Llewellyn, E.J.; Lloyd, N.D.; Degenstein, D.A.; Gattinger, R.L.; Petelina, S.V.; Bourassa, A.E.; Wiensz, J.T.; Ivanov, E.V.; McDade, I.C.; Solheim, B.H.; et al. The OSIRIS instrument on the Odin spacecraft. *Can. J. Phys.* **2004**, *82*, 411–422. [CrossRef]
10. Marynowski, T.; Benzi, E.; Saucke, K.; Mahn, R.; Seidel, J.; Martin Pimentel, P.; Heine, F. Status of the Laser Communication TDP1 Program and its Contribution to Science and Industry. In Proceedings of the 39th International Communications Satellite Systems Conference (ICSSC 2022), Stresa, Italy, 18–21 October 2022. [CrossRef]
11. Heine, F.; Martin-Pimentel, P.; Kaempfner, H.; Muehlnikel, G.; Troendle, D.; Zech, H.; Rochow, C.; Dallmann, D.; Reinhardt, M.; Gregory, M.; et al. Alphasat and Sentinel 1A, the First 100 Links. In Proceedings of the 2015 IEEE International Conference on Space Optical Systems and Applications (ICSOS), New Orleans, LA, USA, 26–28 October 2015; pp. 1–4. [CrossRef]
12. Younus, O.I.; Riaz, A.; Binns, R.; Scullion, E.; Wicks, R.; Vernon, J.; Graham, C.; Bramall, D.; Schmoll, J.; Bourgenot, C. Overview of Space-Based Laser Communication Missions and Payloads: Insights from the Autonomous Laser Inter-Satellite Gigabit Network (ALIGN). *Aerospace* **2024**, *11*, 907. [CrossRef]
13. Giggenbach, D.; Mata Calvo, R.; Mayer, B.; Benthaus, M.; Ivanov, H.; Knopp, M.T.; Saucke, K. Optical Inter-Satellite Links at Lowered Grazing Altitudes for Atmospheric Metrology and Extended Communication Coverage. In Proceedings of the Communications and Observations through Atmospheric Turbulence (COAT 2025), Oberpfaffenhofen, Germany, 7–9 April 2025.
14. Sterr, U.; Dallmann, D.; Heine, F.; Tröndle, D.; Meyer, R.; Lutzer, M.; Benzi, E. Planning Constraints of Low Grazing Altitude GEO–LEO Laser Links Based on In-Orbit Data. *Opt. Eng.* **2016**, *55*, 111608. [CrossRef]
15. Giggenbach, D.; Shrestha, A. Atmospheric Absorption and Scattering Impact on Optical Satellite-Ground Links. *Int. J. Satell. Commun. Netw.* **2022**, *40*, 157–176. [CrossRef]
16. Xu, J.; Rao, L.; Schreier, F.; Efremenko, D.S.; Doicu, A.; Trautmann, T. Insight into Construction of Tikhonov-Type Regularization for Atmospheric Retrievals. *Atmosphere* **2020**, *11*, 1052. [CrossRef]
17. Doicu, A.; Mishchenko, M.I.; Trautmann, T. Electromagnetic scattering by discrete random media illuminated by a Gaussian beam I: Derivation of the radiative transfer equation. *J. Quant. Spectrosc. Radiat. Transf.* **2020**, *256*, 107301. [CrossRef]
18. Doicu, A.; Mishchenko, M.I.; Trautmann, T. Electromagnetic scattering by discrete random media illuminated by a Gaussian beam II: Solution of the radiative transfer equation. *J. Quant. Spectrosc. Radiat. Transf.* **2020**, *256*, 107297. [CrossRef]
19. Kobayashi, T. Reflected solar flux for horizontally inhomogeneous atmospheres. *J. Atmos. Sci.* **1991**, *48*, 2436–2447. [CrossRef]
20. Doicu, A.; Mishchenko, M.I.; Efremenko, D.S.; Trautmann, T. Spectral spherical harmonics discrete ordinate method. *J. Quant. Spectrosc. Radiat. Transf.* **2021**, *258*, 107386. [CrossRef]
21. Evans, K.F. The Spherical Harmonics Discrete Ordinate Method for Three-Dimensional Atmospheric Radiative Transfer. *J. Atmos. Sci.* **1998**, *55*, 429–446. [CrossRef]
22. Evans, K.F. Spherical Harmonic Discrete Ordinate Method (SHDOM) for Atmospheric Radiative Transfer. Available online: https://coloradolinux.com/shdom/ (accessed on 15 June 2026).
23. Doicu, A.; Efremenko, D.S. A Fourier-Space Spherical Harmonic Discrete Ordinate Method for Radiative Transfer in Atmospheres Illuminated by Gaussian Beams. *SSRN* **2026**. [CrossRef]

24. Box, M.A.; Deepak, A. *Small-Angle Approximation to the Transfer of Narrow Laser Beams in Anisotropic Scattering Media*; NASA Contractor Report NASA-CR-3407; National Aeronautics and Space Administration: Washington, DC, USA, 1981.
25. Ishimaru, A. *Wave Propagation and Scattering in Random Media, Vol. 2: Multiple Scattering, Turbulence, Rough Surfaces, and Remote Sensing*; Academic Press: New York, NY, USA, 1978. [CrossRef]
26. Levy, R.C.; Remer, L.A.; Mattoo, S.; Vermote, E.F.; Kaufman, Y.J. Second-generation operational algorithm: Retrieval of aerosol properties over land from inversion of Moderate Resolution Imaging Spectroradiometer spectral reflectance. *J. Geophys. Res. Atmos.* **2007**, *112*, D13211. [CrossRef]
27. Garay, M.J.; Witek, M.L.; Kahn, R.A.; Seidel, F.C.; Limbacher, J.A.; Bull, M.A.; Diner, D.J.; Hansen, E.G.; Kalashnikova, O.V.; Lee, H.; et al. Introducing the 4.4 km spatial resolution Multi-angle Imaging SpectroRadiometer (MISR) aerosol product. *Atmos. Meas. Tech.* **2020**, *13*, 593–628. [CrossRef]
28. Veefkind, J.P.; Aben, I.; McMullan, K.; Förster, H.; de Vries, J.; Otter, G.; Claas, J.; Eskes, H.J.; De Haan, J.F.; Kleipool, Q.; et al. TROPOMI on the ESA Sentinel-5 Precursor: A GMES mission for global observations of the atmospheric composition for climate, air quality and ozone layer applications. *Remote Sens. Environ.* **2012**, *120*, 70–83. [CrossRef]
29. Doicu, A.; Efremenko, D.S.; Wirth, C.L.; Wriedt, T. An algorithm for solving the inverse problem in total internal reflection microscopy. *J. Quant. Spectrosc. Radiat. Transf.* **2025**, *345*, 109534. [CrossRef]
30. Son, H.; Hochstaffl, P.; Efremenko, D.S. Synthetic Study of a Surrogate-Model-Based CO2/CH4 Retrieval Algorithm from Infrared Reflectance Measurements. *Light Eng.* **2026**, *2*, 19–27. [CrossRef] [PubMed]
31. Rao, L.; Xu, J.; Efremenko, D.S.; Loyola, D.G.; Doicu, A. Hyperspectral Satellite Remote Sensing of Aerosol Parameters: Sensitivity Analysis and Application to TROPOMI/S5P. *Front. Environ. Sci.* **2022**, *9*, 770662. [CrossRef]
32. Doicu, A.; Efremenko, D.S. Linearizations of the Spherical Harmonic Discrete Ordinate Method (SHDOM). *Atmosphere* **2019**, *10*, 292. [CrossRef]
33. Budak, V.P.; Korkin, S.V. On the solution of a vectorial radiative transfer equation in an arbitrary three-dimensional turbid medium with anisotropic scattering. *J. Quant. Spectrosc. Radiat. Transf.* **2008**, *109*, 220–234. [CrossRef]
34. Marsaglia, G.; Tsang, W.W. The Ziggurat Method for Generating Random Variables. *J. Stat. Softw.* **2000**, *5*, 1–7. [CrossRef]
35. Matsumoto, M.; Nishimura, T. Mersenne Twister: A 623-dimensionally equidistributed uniform pseudo-random number generator. *ACM Trans. Model. Comput. Simul.* **1998**, *8*, 3–30. [CrossRef]
36. Dong, N.; Wu, C.H.; Ip, W.H.; Chen, Z.Q.; Chan, C.Y.; Yung, K.L. An opposition-based chaotic GA/PSO hybrid algorithm and its application in circle detection. *Comput. Math. Appl.* **2012**, *64*, 1886–1902. [CrossRef]
37. Gao, Y.; Wang, Y.J. A Memetic Differential Evolutionary Algorithm for High Dimensional Functions' Optimization. In *Proceedings of the Third International Conference on Natural Computation (ICNC 2007)*; IEEE: Piscataway, NJ, USA, 2007; Volume 4, pp. 188–192. [CrossRef]
38. Gao, W.F.; Liu, S.Y. A modified artificial bee colony algorithm. *Comput. Oper. Res.* **2012**, *39*, 687–697. [CrossRef]
39. McKay, M.D.; Beckman, R.J.; Conover, W.J. A Comparison of Three Methods for Selecting Values of Input Variables in the Analysis of Output from a Computer Code. *Technometrics* **1979**, *21*, 239–245. [CrossRef]
40. Rahnamayan, S.; Tizhoosh, H.R.; Salama, M.M. Opposition-Based Differential Evolution for Optimization of Noisy Problems. In *Proceedings of the 2006 IEEE International Conference on Evolutionary Computation*; IEEE: Piscataway, NJ, USA, 2006; pp. 1865–1872. [CrossRef]
41. Rahnamayan, S.; Tizhoosh, H.R.; Salama, M.M. Opposition-Based Differential Evolution. *IEEE Trans. Evol. Comput.* **2008**, *12*, 64–79. [CrossRef]
42. Du, Q.; Gunzburger, M.; Ju, L. Advances in studies and applications of centroidal Voronoi tessellations. *Numer. Math. Theory Methods Appl.* **2010**, *3*, 119–142. [CrossRef]
43. Zhang, J.; Sanderson, A.C. JADE: Adaptive Differential Evolution with Optional External Archive. *IEEE Trans. Evol. Comput.* **2009**, *13*, 945–958. [CrossRef]
44. Chuprov, I.; Gao, J.; Efremenko, D.S.; Buzaev, F. Application of Global Optimization for Retrievals from Synthetic Multi-Angle Measurements. *Light Eng.* **2024**, *3*, 11–19. [CrossRef] [PubMed]
45. Tsoulos, I.G.; Lagaris, I.E. MinFinder: Locating all the local minima of a function. *Comput. Phys. Commun.* **2006**, *174*, 166–179. [CrossRef]
46. Dennis, J.E., Jr.; Gay, D.M.; Welsch, R.E. An Adaptive Nonlinear Least-Squares Algorithm. *ACM Trans. Math. Softw.* **1981**, *7*, 348–368. [CrossRef]
47. Dennis, J.E., Jr.; Gay, D.M.; Welsch, R.E. Algorithm 573: NL2SOL—An Adaptive Nonlinear Least-Squares Algorithm. *ACM Trans. Math. Softw.* **1981**, *7*, 369–383. [CrossRef]
48. Byrd, R.H.; Lu, P.; Nocedal, J.; Zhu, C. A Limited Memory Algorithm for Bound Constrained Optimization. *SIAM J. Sci. Comput.* **1995**, *16*, 1190–1208. [CrossRef]

49. Morozov, V.A. *Methods for Solving Incorrectly Posed Problems*; Springer: New York, NY, USA, 1984. [CrossRef]
50. Ramlau, R. Morozov's Discrepancy Principle for Tikhonov Regularization of Nonlinear Operators. *Numer. Funct. Anal. Optim.* **2002**, *23*, 147–172. [CrossRef]